



Implication of nano-scale grain refinement by severe shot peening on corrosion resistance of additively manufactured 316 L stainless steel

P. Ebrahimzadeh^{a,*}, L.B. Peral^{a,*} , R. González-Martínez^b , E. Mardaras^b , I.I. Cuesta^c, I. Fernández-Pariente^a

^a Department of Material Science and Metallurgical Engineering, University of Oviedo, Gijón, Spain

^b AZTERLAN, Basque Research and Technology Alliance (BRTA), Durango, Spain

^c Department of Civil Engineering, University of Burgos, Burgos, Spain

ARTICLE INFO

Keywords:

Selective Laser Melting, Shot Peening
Grain refinement
EBSD
Corrosion

ABSTRACT

Microstructural analysis and electrochemical measurements were performed in a SLM 316 L steel that was submitted to SSP. In comparison to the wrought steel, the greatly smaller grain size and higher dislocation density promote nucleation sites for oxidation, and a thicker passive layer, with more stable Cr₂O₃ oxides, is formed on the SLM steel. SSP produces a thick-gradient surface layer with a nanostructured surface. Overall corrosion resistance decreased in comparison to the un-peened SLM. SSP induces decohesion along the MPBs, leading to pitting. High-residual stresses, twins and dislocation break the cellular-walls, promoting the imperfect cell-structure and jeopardizing the passive film stability.

1. Introduction

Austenitic stainless steels (ASS) are widely employed in automotive, aerospace and medical equipment, due to its excellent mechanical properties and corrosion resistance [1,2]. Nevertheless, mechanical and corrosion behavior of ASS must be further studied because of the impending use of the new additive manufacturing techniques in the industrial field.

Selective Laser Melting (SLM) is an additive manufacturing method that melts powdered raw material by means of a high energy laser beam, before its solidification. It offers the advantage to produce complex alloys parts that can not be manufactured by conventional methods. Besides, previous studies have demonstrated that SLM ASS show superior mechanical properties than conventional wrought ASS [3]. However, further research is still needed in terms of corrosion properties of the additively manufactured ASS [4].

SLM 316 L susceptibility to the different forms of corrosion are now being investigated by the scientific community to qualify SLM ASS for industrial service. The microstructures produced by SLM are related to the process parameters, such as laser power, laser scanning speed, layer thickness and hatch distance, revealing the importance of parameter optimization in the SLM process.

Porosity is one of the key factor that influences corrosion resistance

of SLM 316 L. Sun et al. [5] revealed that porosity will have a preferential pit initiation if it is more than 1 %. In that same context, Sander et al. [6] reported that SLM 316 L samples with porosities ranging around 0.04–0.05 % showed notable pit initiation resistance in comparison to wrought 316 L. In SLM 316 L, Chao et al. [7] have also reported that the improved pitting resistance is attributed to the annihilation of detrimental manganese sulphide (MnS) inclusions, benefiting from the high solidification velocity of additive manufacturing (~10⁷ K/s). Previously, Zhang et al. [8] revealed that MnS inclusions are unavoidable in conventional 316 L and they facilitate initiation of pitting corrosion. Based on these findings, Ni et al. [3] reported that pitting potentials of the SLM 316 L were higher than those of the wrought samples, in chloride solutions with different concentrations. Zietala et al. [9] informed that pitting potential in SLM 316 L was around 300 mV positive than its wrought counterpart in 3.5 wt% NaCl solution. Kong et al. [10] have also found that the pitting potential of the SLM 316 L is over 1 V exceeding the typical value of 0.3 V for conventional 316 L. However, the pitting potential and the passive film thickness decreased after heat treatment at 1050°C and especially, at 1200°C. This fact was attributed to the compressive residual stress relief and decrease in dislocation density. In SLM process, high dislocation density present at the cellular boundaries improves diffusion and electron activity, decreasing the energy barrier for electrochemical reactions

* Corresponding authors.

E-mail addresses: UO286172@uniovi.es (P. Ebrahimzadeh), luisborja@uniovi.es (L.B. Peral).

<https://doi.org/10.1016/j.corsci.2024.112628>

Received 14 August 2024; Received in revised form 12 November 2024; Accepted 9 December 2024

Available online 10 December 2024

0010-938X/© 2024 The Authors. Published by Elsevier Ltd. This is an open access article under the CC BY-NC-ND license (<http://creativecommons.org/licenses/by-nc-nd/4.0/>).

Table 1
Chemical composition (wt%).

Series	C	Si	Mn	Cr	Ni	Mo
Wrought & annealing	0.021	1.00	2.00	17	12	2.25
SLM	0.020	0.60	1.20	18	12	2.00

Table 2
Printing parameters. Selective Laser Melting technique.

Laser power (W)	Scanning speed (mm/s)	Hatching distance (mm)
225	650	0.1

Table 3
Characteristics of the peening media.

Shot type	Material	Nominal diameter	Hardness (HB)
round shots	ASS	0.6	150

Table 4
Almen intensity characterization.*Peening flux rate is controlled by the peening valve opening in the Guyson Euroblast shot peening machine.

Pressure (bar)	Peening flux rate*	Peening height (mm)	Peening angle (°)	Shot type
2	2 turns	230	90	Table 3

Table 5
Shot peening.

	Almen intensity	Surface coverage (%)	Exposure time (s)
CSP	12 A	100	7
SSP	12 A	3000	210

what promotes the formation of a thicker passive layer. The effect of residual stress on the corrosion resistance of 316 L manufactured by SLM was also studied by V. Cruz et al. [11]. They informed that pitting potential increased and passive film current decreased, with increasing compressive stresses. This fact, associated with the slightly interatomic distances into the compressively stressed lattice, was attributed to the formation of a robust passive layer. Nevertheless, the compressive residual stresses influenced the repassivation potential detrimentally. The poorer repassivation properties were associated to the sluggish passive film growth kinetics. Although there is a general consensus about the positive influence of externally introduced compressive residual stresses on corrosion resistance, the role of residual stresses on the passivity of SLM counterparts needs to be better explored. J. Sun et al. [12] informed that ultrasonic severe surface rolling (USSR) produced a gradient surface layer with a grain size of 86 nm in the top surface layer that contributes to improve corrosion resistance of selective laser melted 316 L, in 3.5 wt% NaCl solution. Y. Zhao et al. also [4] stated that the small grain size and high grain boundaries density enhance the formation of stable oxides, resulting in high corrosion resistance. Recently, P. Ebrahimpzadeh et al. [13] informed that severe shot peening (SSP) with subsequent low annealing treatment can be employed to increase corrosion resistance of 316 L in 3.5 wt% NaCl solution. Authors also informed that corrosion behavior is strongly dependent on the effects of work hardening and microstructural singularities promoted by severe peening. SSP promotes grain refinement, work hardening and the formation of strain-induced martensite, improving hardness near surface areas. However, certain discrepancies have been reported in literature on the positive or negative role of shot peening in corrosion resistance of 316 L. Even though SSP is known, its response to corrosion is still a work in progress.

Studying corrosion behavior of shot peened SLM printed 316 L has attracted limited attention and corrosion mechanisms have not been systematically studied yet. To the author's best knowledge, understanding the relationship processing parameters, shot peening and corrosion becomes critical in producing SLM printed 316 L components. Thus, in this study, selective laser melted 316 L samples were submitted to conventional (CSP) and severe shot peening (SSP) treatments. The shot peened samples (as-built + CSP and as-built + SSP) and reference (SLM as-built) were characterized including phases, grain refinement, surface and subsurface residual stresses and work hardening (Full Width at Half Maximum) and microhardness profiles. Electrochemical tests, including potentiodynamic polarizations and electrochemical impedance (EIS) were also performed to evaluate corrosion behavior of as-built and as-built + SSP selective laser melted samples. Results were compared with its wrought equivalent, in 3.5 wt% NaCl.

2. Experimental procedure

2.1. Material and selective laser melting (SLM) technique

The chemical composition of both wrought and SLM 316 L is given in Table 1. The common processing parameters based on the manufacturer's recommendations were used in this study (Table 2). Anyway, the selected printing parameters are also discussed in further section. SLM series showed a relative density of 98 % measured by means of Archimedes method.

2.2. Shot peening treatment and surface condition

In the present study, conventional (CSP) and severe shot peening (SSP) treatment were applied on SLM 316 L by means of an air Euroblast 4 PF Shot Peening machine. The peening media characteristics are given in Table 3. Initially, Almen characterization was performed, following the conditions described in Table 4. Almen intensity was calculated from the Almen saturation point, using A strips. The Almen saturation intensity was found to be 12 A. For more information, the reader is addressed to [13].

Once Almen intensity was characterized, coverage factor (C) was determined, according to Eq. 1. Selective laser melted samples were always blasted with an Almen intensity of 12 A. Shot peening with 100 % coverage was considered as conventional shot peening, while shot peening with 3000 % coverage was considered as severe (Table 5).

$$C (\%) = 100 \cdot [1 - \exp(-A \cdot t)] \quad (1)$$

In this work, the studied series are divided in: as-built, as-built + CSP and as-built + SSP. Results are compared with those determined in a conventionally manufactured austenitic steel, denoted as wrought + annealing.

It is well known that SSP can promote grain refinement, work hardening as well as martensitic phase transformation [13–16]. Although the influence of severe plastic deformation in microstructure and corrosion resistance of conventionally manufactured ASS has been extensively studied [13,17–19], the SSP response of additively manufactured 316 L is still a work in progress, especially in terms of corrosion properties and mechanisms. Even, contradictory points of view have been found in literature about the role of grain refinement induced by cold-working on corrosion resistance. While Q. Xu et al. [20] and J. Sun et al. [12] argued that nanocrystallization is beneficial in terms of corrosion resistance, other authors have reported the opposite effect [21,22]. Focusing on the influence of severe deformation processes able to promote the formation of nanocrystalline structures, in series subjected to SP, corrosion studies were only conducted in the as-built + SSP samples. After applying the SSP and to remove any contaminant adhering to the surface, all samples were rinsed ultrasonically in acetone and distilled water successively, for 20 minutes.

To study the influence of mechanical and microstructural

Table 6
Surface roughness (μm) after polishing.

	R_a	R_z	R_{max}
Wrought + annealing	0.15 ± 0.04	1.3 ± 0.60	1.90 ± 0.5
SLM as-built	before polishing	6.58 ± 1.40	8.3 ± 1.72
	after polishing	0.14 ± 0.03	1.3 ± 0.40
as-built + SSP	before polishing	5.00 ± 1.00	24.0 ± 2
	after polishing	0.13 ± 0.05	1.3 ± 0.50

singularities on corrosion resistance, without the interference of the surface roughness [13,23], all the samples were polished, by 1200 SiC paper. In the case of the as-built + SSP series, mechanical polishing was carefully performed, without noticeably altering the refined surface layer induced by the high-energy (12 A and 3000 % coverage) delivered onto the steel surface. Surface roughness values are given in Table 6. ' R_a ' is the average roughness, ' R_z ' represents the average maximum height of the profile and ' R_{max} ' is the maximum roughness depth. Measurements were conducted using a DIAVITE DH-6 roughness tester.

2.3. Microstructural characterization

The phase of the wrought and additively manufactured samples were analyzed by means of a Seifert XRD 3000 T/T diffractometer, with a Mo-K α radiation source at 40 kV and 40 mA. The scanning range was from 7 to 37 $^\circ$ in 2 θ , with a step size of 0.025 $^\circ$ and 60 s per point.

To reveal the microstructural features, the samples were metallographically prepared. They were ground up to 1200 SiC paper, and

polished with 6 and 1 m diamond paste. Then, they were electrochemically etched in a 5 wt% oxalic acid solution, at a DC voltage of 7 V for 50 s. Microstructure was observed in a SEM JEOL JSM 5600.

Microstructural analysis was completed by EBSD technique with a EBSD detector (Symmetry) from Oxford instruments. Analysis was carried out to analyze the grain size and the geometrically necessary dislocation density (GND). In samples subjected to SP, EBSD analysis was conducted on the cross-sectional samples. EBSD data were acquired withing 150 x 150 μm^2 area with a step size of 300 nm. In the case of the shot peened surfaces, a finer scan of 30 nm was employed to analyze the grain refinement level promoted by the CSP and SSP treatments, in an area of 5 x 25 μm^2 . The EBSD data were analysed with AZtecCrystal software. The average density of geometrically necessary dislocations (GND) was calculated using the approach described in [24]. It was assumed that GNDs is linearly dependent on the Kernel Average Misorientation (KAM) value according to Eq. 2. The selective laser melted samples show orientation gradients and these orientation gradients are displayed by means of a KAM map. The dislocation density corresponds to the colour legend, with blue areas having the lowest and the green areas having the highest density.

$$\rho_{GND} = \frac{\theta_{true}}{b \cdot n \cdot a} \quad (2)$$

where θ_{true} is the true KAM value, b is the length of the Burgers vector, n is the size of the Kernel, measured in a number of EBSD measurement steps and a is the measurement step size.

The magnitude and depth of the hardening caused by the shot peening were determined in a Buehler Micromet 2100. A force of 200 g

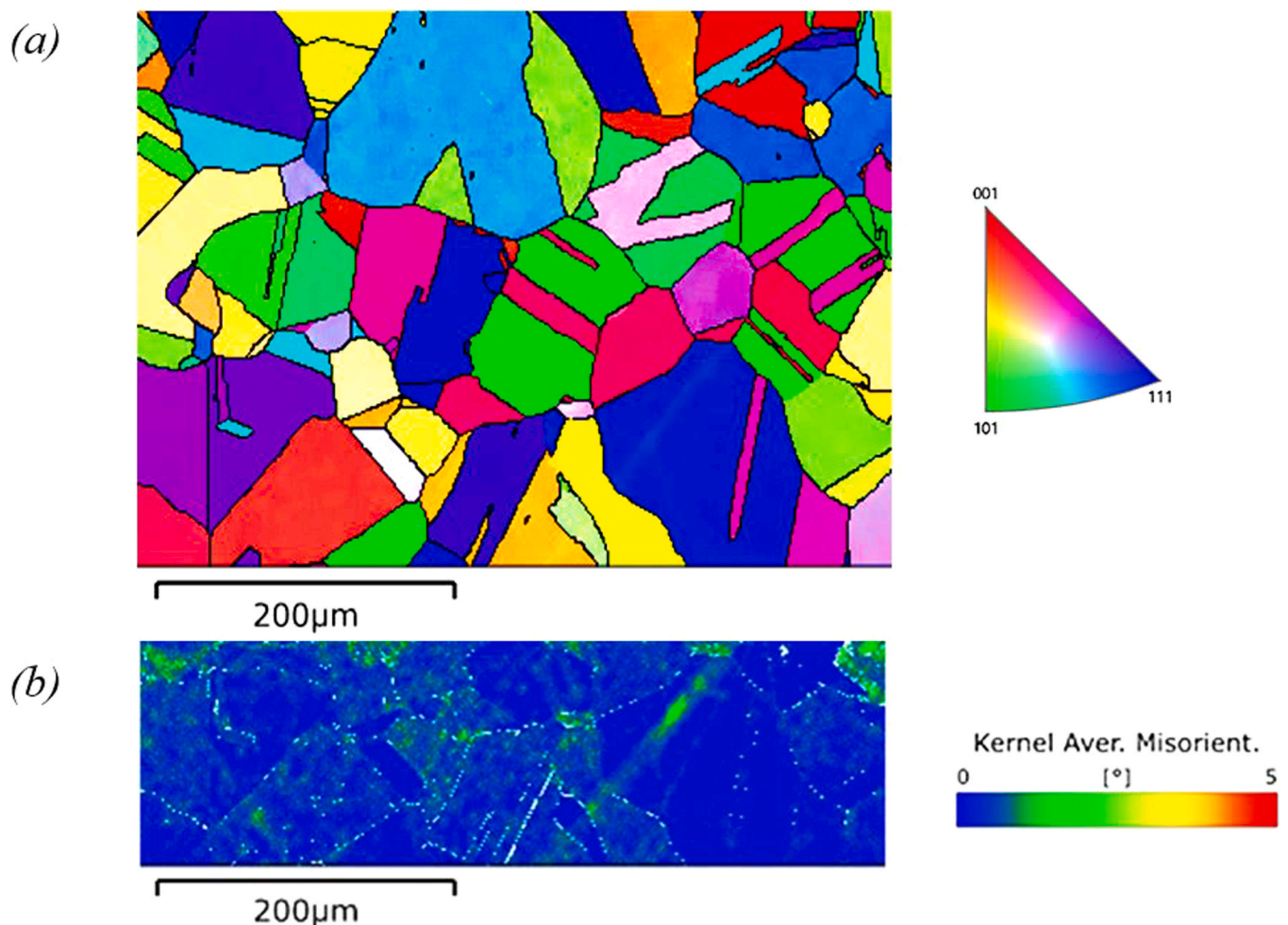
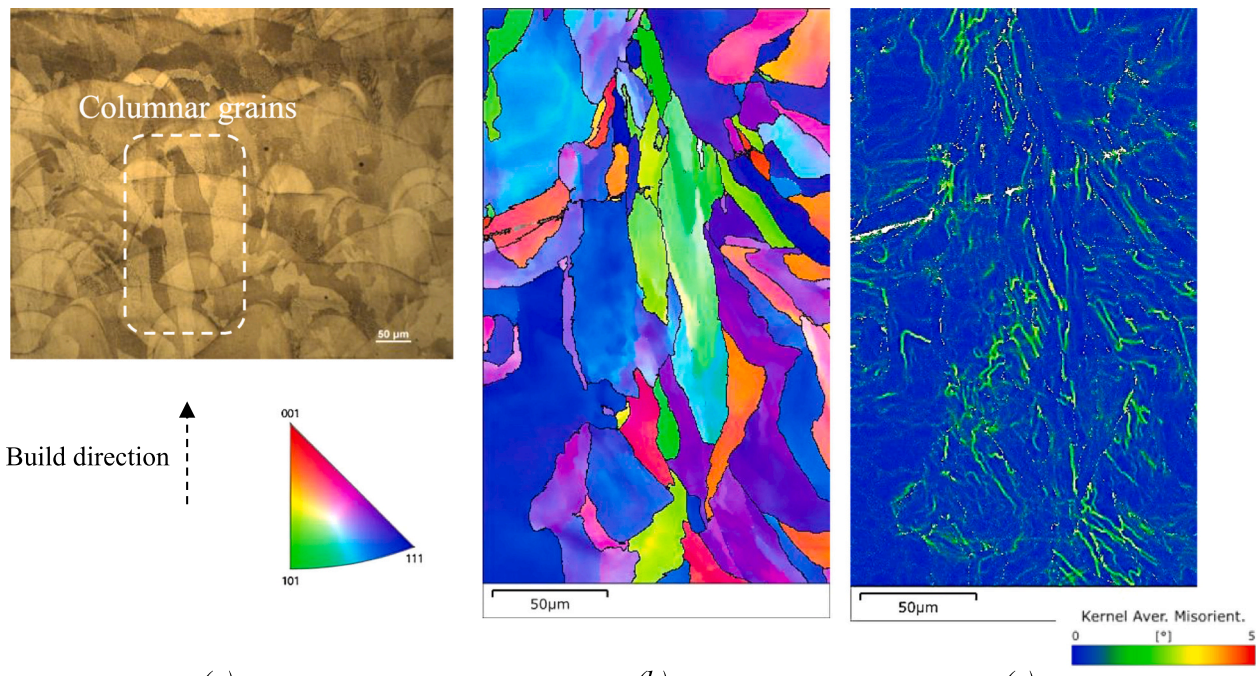


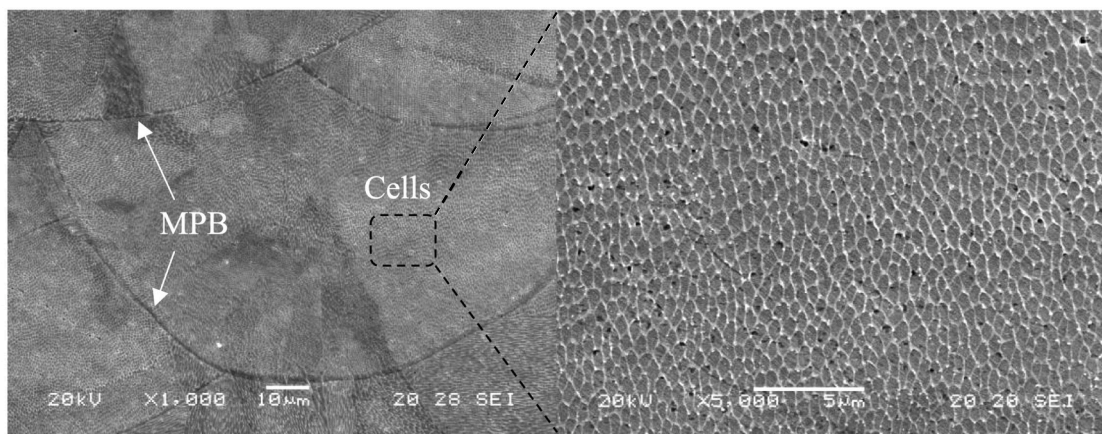
Fig. 1. Microstructure of the wrought + annealing series. (a) Inverse pole figure obtained via EBSD. (b) KAM results.



(a)

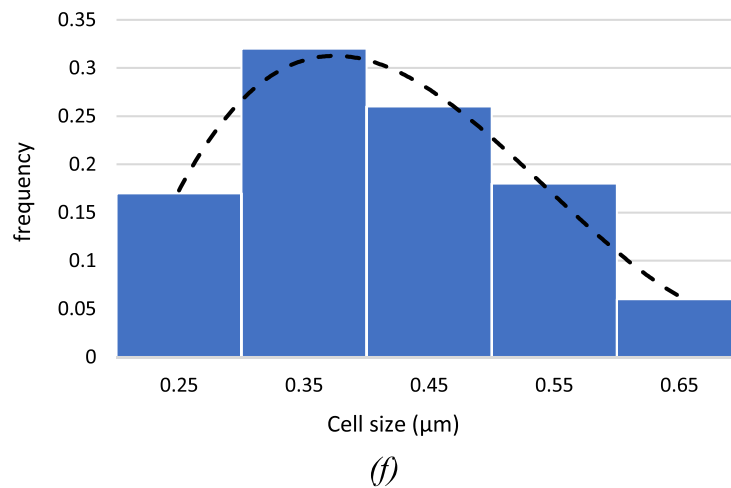
(b)

(c)



(d)

(e)



(f)

Fig. 2. Microstructure. Selective laser melting series: as-built condition.

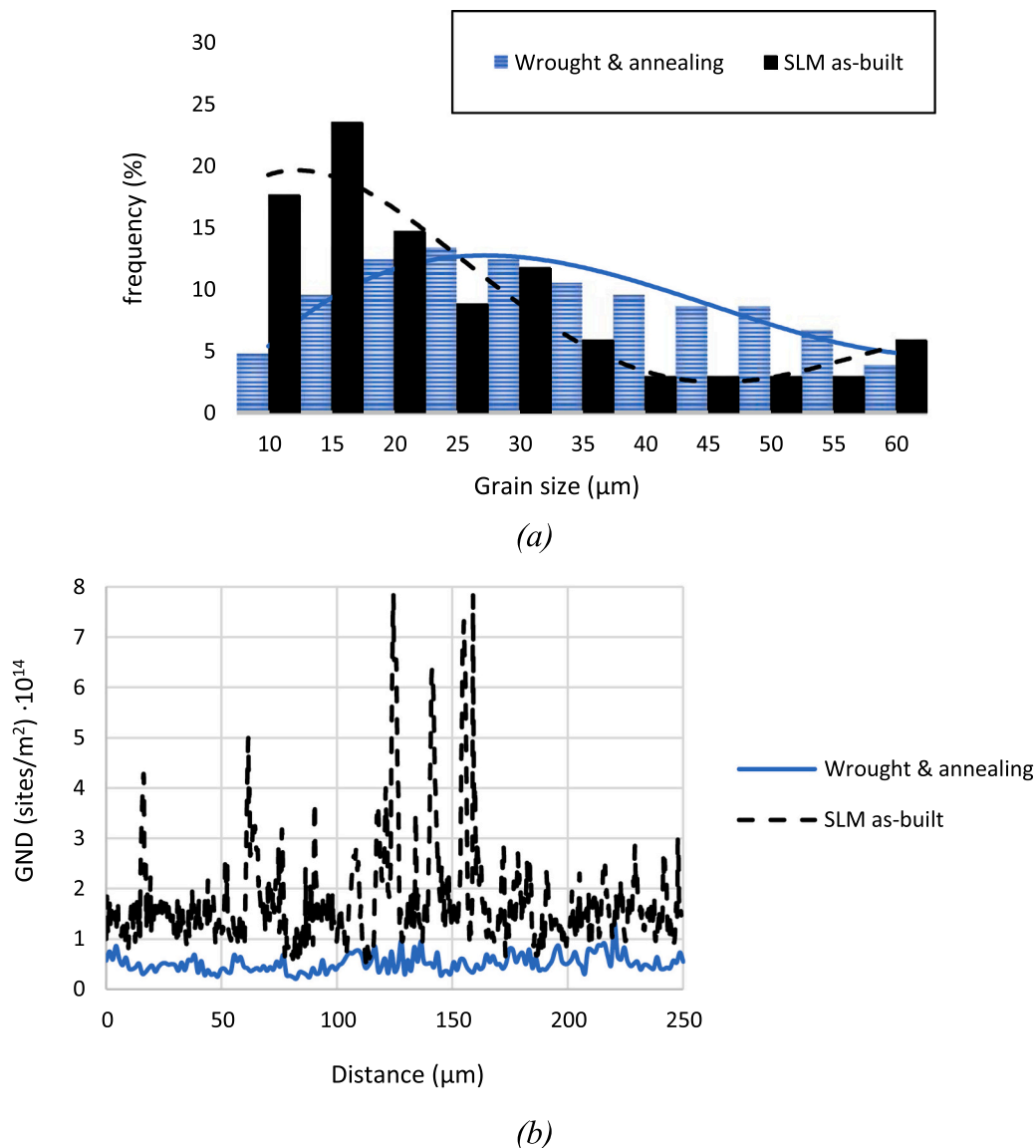


Fig. 3. (a) Grain size and (b) dislocation density distribution.

was applied for 15 s. The measurements were conducted from the surface to sample's core. Full Width at Half Maximum (FWHM) parameter and the residual stress profiles were also measured in a Stresstech 3000-G3R X-ray diffractometer. FWHM (i.e. work hardening index) is related to grain distortion, dislocation density and residual micro-stress state [13,25]. Residual stresses was determined using the $\sin^2\psi$ technique. The $K\alpha$ chromium wavelength was used onto the {200} gamma lattice plane, under a 2θ of 128.8° [13]. Residual stresses and FWHM were analyzed in depth. For that, an electrochemical process was applied, using a potential of 45 V and a reactive agent composed by 96 % acetic acid and 4 % perchloric acid.

2.4. Electrochemical measurements

Electrochemical behavior of the wrought + annealing and selective laser melted samples (as-built and as-built + SSP) was analyzed by PalmSens4 potentiostat. Electrochemical measurements were conducted in 3.5 wt% NaCl solution at room temperature, by using a traditional three electrode system. The working electrode was the test sample, the counter electrode was a platinum sheet ($20 \times 20 \text{ mm}^2$) and the reference electrode was a saturated Ag/AgCl electrode. The open circuit potential

(OCP) was monitored for two hours until stable OCPs was achieved. Potentiodynamic polarization tests were performed in the range -0.2 V from the OCP to $+1 \text{ V}$ at a scan rate of 0.6 V/h . EIS measurements were conducted in a range of frequency varying from 100 kHz to 10 mHz with $\pm 10 \text{ mV}$ sweep from the OCP. Potentiostatic polarization were measured at a constant potential of $+0.25 \text{ V}$ from the OCP, for 20 min.

The chemical compositions and elemental state of the passive film on wrought + annealing, as-built and as-built + SSP samples after $+0.25 \text{ V}$ potentiostatic polarization for 20 min were determined by XPS (X-ray Photoelectron Spectroscopy) analysis. XPS measurements were carried out using a Phoibos hemispherical analyser, with monochromatized $K\alpha$ Al radiation (1486.74 eV). High resolution spectra were taken using 30 eV energy pass and 0.1 eV energy step. The composition ratio in the passive layer was calculated by integrating the corresponding area. After the potentiostatic polarization tests, the surface topography was also analyzed in a Confocal Spectral Leica TCS-SP8X microscope.

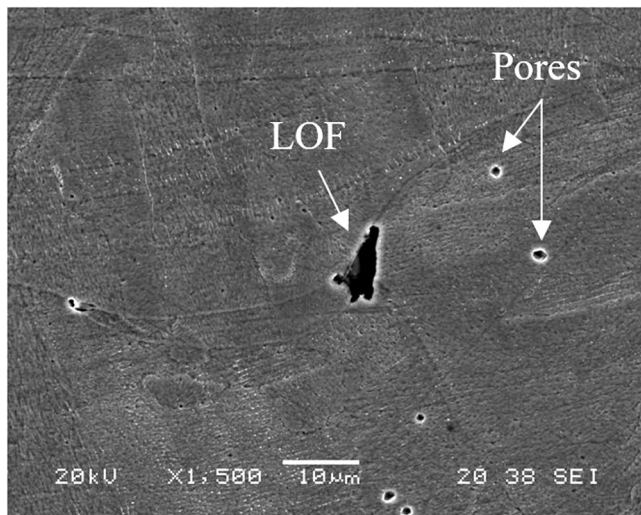


Fig. 4. Defectology in selective laser melting series: as-built condition.

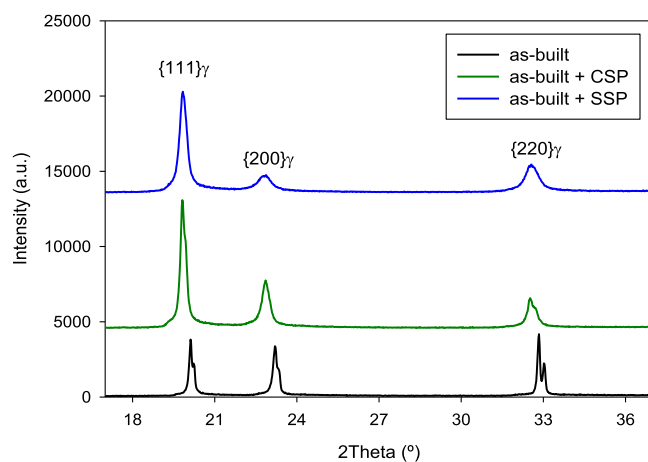


Fig. 5. XRD patterns for the different series onto the surface layer.

3. Results

3.1. Microstructure: wrought and annealing and SLM series

The microstructure of the wrought and annealing 316 L can be observed in Fig. 1(a). It consists on regular austenitic polygonal grains in the range of 10–60 μm . Fig. 1(b) shows the kernel average misorientation (KAM) evolution for the wrought and annealed series. The 316 L samples prepared by SLM shows the fan-shaped melt pools (Fig. 2(a) and (d)) caused by the incremental layer by layer SLM construction process. The as-built microstructure is composed of columnar grains forming epitaxially along the build direction (Fig. 2b). SLM 316 L has a wider size range of irregular grains, where most grains have a size of around 10–15 μm (Fig. 3(a)).

Fig. 2e displays that many subgrains (cellular structure) with an average size of 400 nm (Fig. 2f) exist in the SLM 316 L series, which can be attributed to the high dislocation density due to the rapid solidification, during the printing process. The average of geometrically necessary dislocations (GND) was found to be $0.5 \cdot 10^{14} \text{ m}^{-2}$ in the wrought and annealed series, and $1.5 \cdot 10^{14} \text{ m}^{-2}$ in the SLM 316 L series, Fig. 3(b). A very high stress level was confirmed after printing (Fig. 2c).

Incomplete fusion holes and spherical porosities randomly distributed in microstructure were very locally observed (Fig. 4). Incomplete fusion holes, i.e. lack of fusion (LOF) defects, are generally attributed

to the lack of energy input during the SLM process. Energy input (E) can be estimated according to Eq. 3, where ' P ' is laser power (W), ' v ' is can speed (mm/s), ' h ' is hatching distance (mm) and ' t ' is layer thickness (mm).

$$E = \frac{P}{v \cdot h \cdot t} \quad (3)$$

Therefore, an energy density of 70 J/mm^3 can be calculated. An energy density exceeding 60 J/mm^3 contributes to minimize the defects during the SLM process, resulting in low density of defects (less than 1 %) when an appropriate energy input is utilized [26]. This fact contribute to explain that LOF defects and porosity have been observed in very local areas. G. Álvarez et al. [27] also observed the presence of pores and LOF defects in additively manufactured 316 L stainless steel. As in this work, the presence of defects was also reported to be less than 1 %, in the as-built condition. Although pores are difficult to avoid, it can be controlled to a extremely low levels by selecting the right energy input (70 J/mm^3 in the present study). Porosity is one of the factors that influence corrosion resistance of SLM 316 L. Nevertheless, several authors [28,29] have suggested that porosity would not have a preferential pit initiation if it was less than 1 %. Although mechanical and microstructural singularities that affect SLM 316 L corrosion resistance will be discussed later, the printing parameters were selected to minimize the presence of defects, which could have a negative impact on corrosion resistance.

3.2. Influence of plastic deformation on microstructure of selective laser melting series: as-built + CSP and as-built + SSP

The XRD profiles for the SLM series are shown in Fig. 5. The SLM series did not have martensitic peaks, even for the severe shot peening series. In a previous work, P. Ebrahimzadeh et al. [13] shown martensitic peaks for the severely peened samples in the wrought and annealed 316 L. In the present work, the absence of martensite after plastic deformation is attributed to the strongly oriented grain structure in SLM series (Fig. 2b and Fig. 6) which could be more resistant to plastic deformation than the wrought and annealed series.

XRD analysis in the shot peened samples (CSP and SSP) resulted in high broadening of peaks. This fact is associated to the increase of dislocation and formation of surface subgrains. Fig. 6(a) and (b) displays the KAM results and the inverse pole figures of the CSP and SSP SLM 316 L samples, respectively. As can be seen, SLM as-built + CSP and SLM as-built + SSP exhibited a very high stress status in comparison to the un-peened one, which is attributed to the bombardment of shot peening media. It is evident from the figure that the depth of the affected layer by the shot peening increased after the severe bombardment, with a coverage level of 3000 %. Bombardment of shot peening media promoted plastic deformation and therefore, GND density increased near the surface (Fig. 6c). This effect was especially notable in the SLM as-built + SSP sample.

The difference between deformed grain regions among the different series can be observed from the IPF maps. The grain refinement depth of 50 μm was observed after the conventional shot peening. However, it increased to 100 μm with the severe shot peening. A careful observation by using a smaller step size enables higher indexing success. Hence, the smallest grains near the top surface region could be observed. The difference in grain refinement is also displayed in Fig. 6(d). In the case of the CSP samples, grains have a size of around 0.2–1 μm . However, nano (grains smaller than 100 nm) and submicron sized grains were observed in the severely peened samples, very near the top deformed region. The grain size gradually increases in depth, being similar again to that determined in the un-peened as-built samples. The un-peened as-built sample had an average hardness of 260HV, while hardness increased to 350HV and 420HV after the CSP (100 % coverage) and SSP (3000 % coverage) treatments, respectively (Fig. 7). In addition, the shot peening promoted hardness depth is around 200 μm , after which the hardness

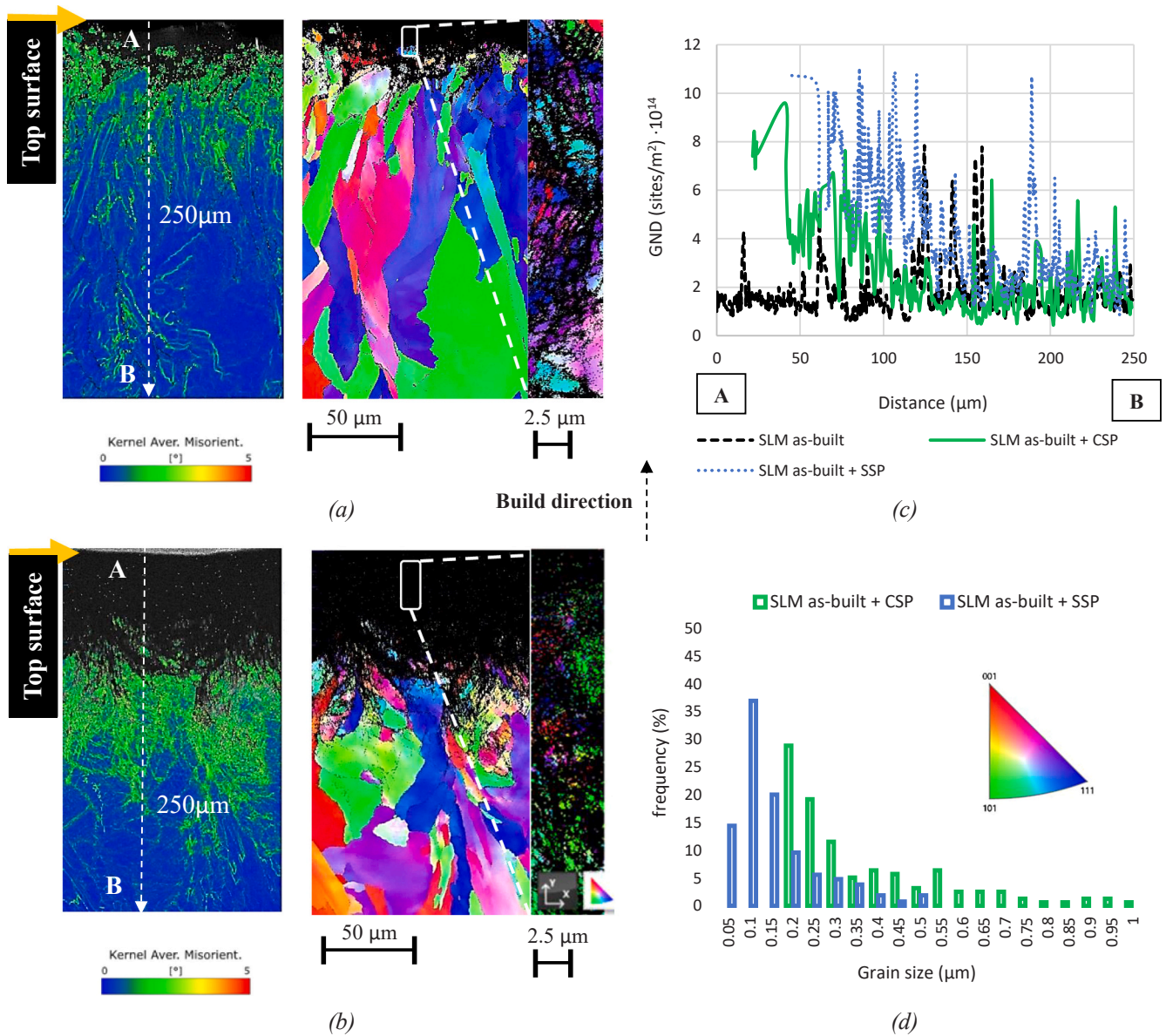


Fig. 6. (a) as-built + CSP (transversal section), (b) as-built + SSP (transversal section), (c) GND density in all series and (d) grain refinement level near the surface.

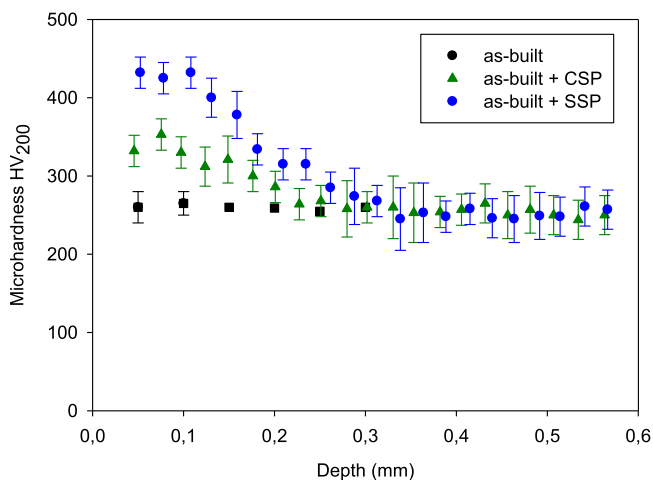


Fig. 7. Microhardness profile in depth.

reach the un-peened sample value. It is important to mention that the hardness of SSP sample was improved by 62 %. This effect is attributed to work hardening along with grain refinement. As previously mentioned, after SSP, GND increased to 10^{15} m/m³ and grains smaller than 100 nm were identified near the surface.

The residual stresses of the un-peened and shot-peened samples are given in Fig. 8(a). CSP and SSP treatments induced larger compressive residual stresses. In comparison to the CSP treatment, the SSP series induced higher and deeper compressive residual stresses. In this case, compressive residual stresses of more than -600 MPa up to 100 μm depth were determined by X-Ray diffraction. The full width Half maximum (FWHM) is depicted in Fig. 8(b). FWHM increased after shot peening, especially after the high plasticity induced during the severe bombardment. As previously stated, KAM results already evidenced a very high stress level after the severe shot peening (3000 % coverage). The IPF maps (Fig. 9) shows a gradual increase in grain size, starting from nano-scale, highly refined grains at the top surface, progressing to coarser grains throughout the core material, especially after the SSP. It is important to note that the black areas correspond to nanostructured grains, smaller than 100 nm, which were undetectable due to the EBSD

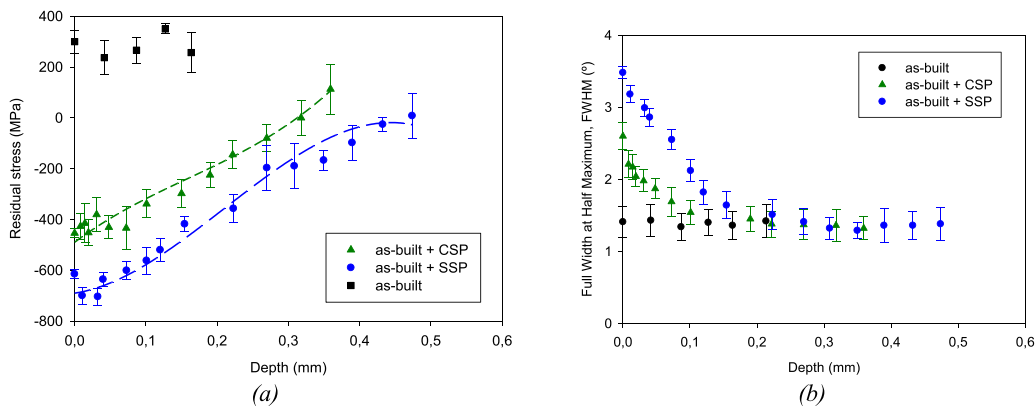


Fig. 8. (a) Residual stresses and (b) FWHM evolution in depth in as-built series (SLM), as-built + CSP and as-built + SSP.

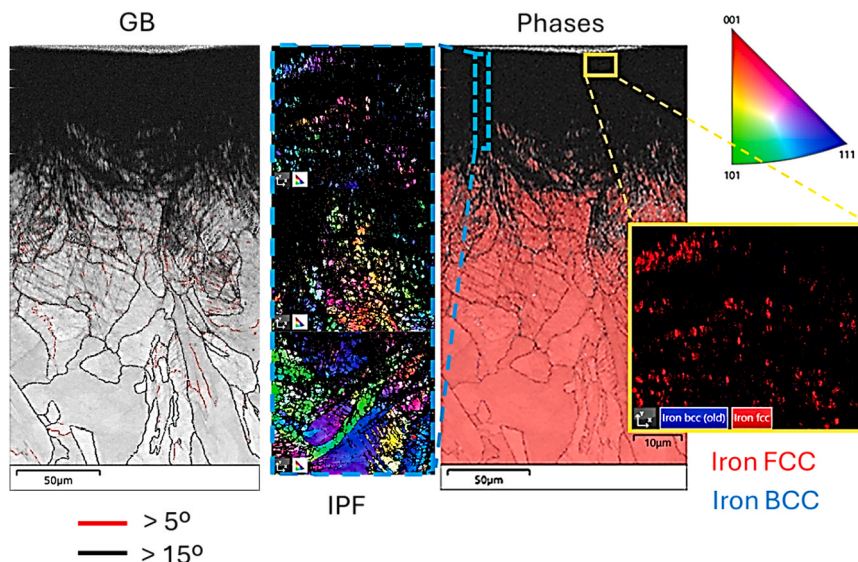


Fig. 9. Obtained results from EBSD analysis in terms of GB, IPF and phase maps in as-built + SSP sample.

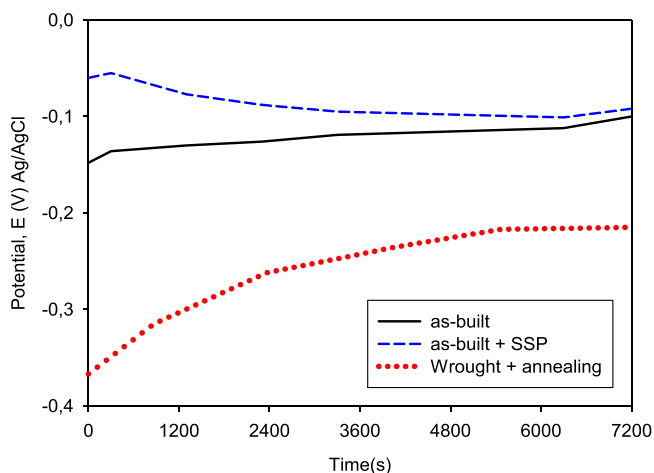


Fig. 10. Open Circuit Potential evolution in 3.5 wt% NaCl solution for 2 h.

scanning step size.

The crystallite size, using the FWHM parameter, was calculated by means of the Williamson-Hall method [30]. The crystallite size of the top surface of samples subjected to SSP was ≈ 10 nm. These results clearly show that surface nanocrystallization occurred in as-built + SSP

samples, with crystallite sizes below 100 nm. Among the treatments, SSP demonstrated the greatest effectiveness in reducing grain size, indicating superior grain refinement (Fig. 6 and Fig. 9). The findings also reveal that specimens treated with SSP had the highest KAM values. KAM values, around 5°, were well correlated with the depth of refined grains, while lower KAM values, around 1°, correspond to the less deformed areas. Besides, in the very top surface layer, the phase map revealed a continuous austenite phase (Fig. 9). The presence of the strain-induced martensite was not detected from the EBSD analysis. This analysis is consistent with the results obtained from the XRD analysis (Fig. 5), demonstrating strong alignment between the two characterization techniques, and confirming the absence of martensite. The absence of martensite, after applying the SSP treatment in the SLM samples, is mainly attributed to strongly orientated grain structure which is more resistant to plastic deformation. A similar finding was previously reported by T. Gundgire et al. [31]

3.3. Electrochemical measurements

3.3.1. Open Circuit Potential (OCP) and potentiodynamic polarization curves

Fig. 10 shows the OCP evolution for two hours in 3.5 wt% NaCl. The OCPs become practically changeless after 4800 s and remain constant the following time. The E_{OCP} value of the wrought + annealing series decreased (≈ -0.22 V) in comparison to the additively manufactured

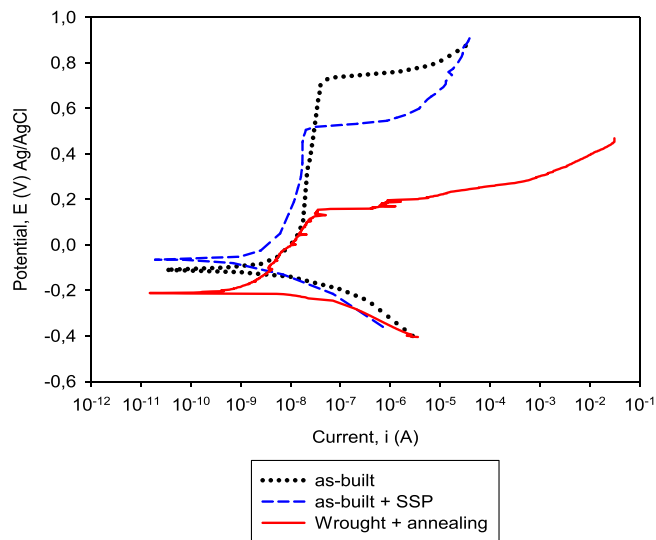


Fig. 11. Potentiodynamic polarization curves in 3.5 wt% NaCl solution at RT.

Table 7

Electrochemical parameters extracted from the potentiodynamic polarization curves.

Series	E_{corr} (V)	E_{pit} (V)	$E_{\text{pit}} - E_{\text{corr}}$ (V)	i_{pass} ($\mu\text{A}/\text{cm}^2$)
Wrought + annealing	-0.21	0.13	0.34	0.04
SLM as-built	-0.11	0.73	0.84	0.06
SLM as-built + SSP	-0.07	0.50	0.57	0.02

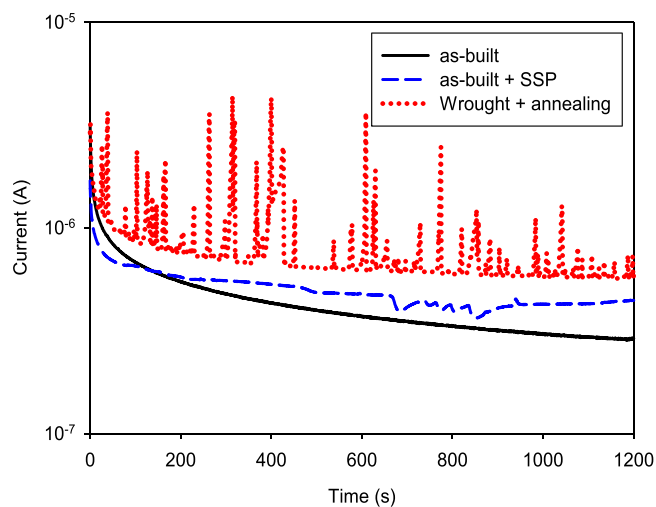


Fig. 12. Current evolution as a function of time at +0.25 V from the OCP in 3.5 wt% NaCl.

series (≈ -0.1 V). The SLM samples (as-built and as-built + SSP) showed a higher E_{OCP} value. As will be seen later, the higher OCP value indicated that material is less prone to corrosion, in other words, the increase of OCP value evidences that the increased compactness of passive film with time [32,33].

The potentiodynamic polarization curves of the wrought + annealing and SLM series are displayed in Fig. 11. There is no clear difference among the three cathodic polarization branches. Self-passivation characteristics in 3.5 wt% NaCl were clearly noted for both additively manufactured series and wrought + annealing. To evaluate passivation properties, polarization curves were analyzed and

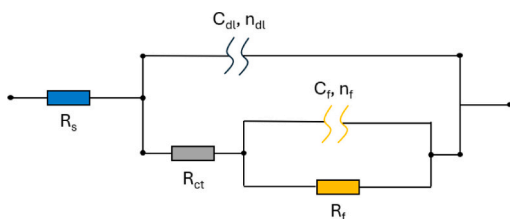
Table 8

Corrosion parameters obtained from the EIS measurements. χ^2 stands the fitting deviation in the equivalent circuit analysis.

	Wrought + annealing	SLM as-built	SLM + SSP
R_s (Ohm)	2.4	1.5	1.4
C_{dl} ($\mu\text{F}/\text{cm}^2$)	75	40	63
n_{dl}	0.85	0.92	0.9
R_{ct} (Ohm)	40,000	94,000	62,000
C_f ($\mu\text{F}/\text{cm}^2$)	100	36	75
n_f	0.74	0.91	0.84
R_f (Ohm)	70,000	320,000	10^5
χ^2 (error)	< 0.1	< 0.1	< 0.1

the obtained electrochemical parameters are given in Table 7. SLM series (as-built and as-built + SSP) and wrought + annealing evidenced minimal differences (≈ 20 – 60 nA/cm²) in passive current density (i_{pass}). However, pitting potential (E_{pit}) and the potential range from corrosion to pitting potential ($E_{\text{pit}} - E_{\text{corr}}$) were other critical parameter to analyze passivation behavior. $E_{\text{pit}} - E_{\text{corr}}$ range (passivity range) in SLM as-built series (840 mV_{Ag/AgCl}) was wider than wrought + annealing series (340 mV_{Ag/AgCl}). Accordingly, corrosion resistance of SLM as-built series is higher than that of the wrought + annealing series. Besides, metastable pitting current peaks were also observed in wrought + annealing series, before reaching the pitting potential. As mentioned previously, in the SLM 316 L, the low porosity (below 1 % in this study) and the pore size smaller than 2 μm (Fig. 4) do not appear to compromise the passive film stability. In this regard, Schaller et al. [34] observed that the reduced corrosion resistance, in chloride solution, of SLM stainless steels took place at large pores with diameters exceeding 50 μm . On the other hand, D.C. Kong et al. [35] also stated that in SLM 316 L stainless steel, pores with diameters below 10 μm can be corroded in more aggressive environments, such as sulfuric acid. Thus, in our study, porosity does not seem to play a mayor role on corrosion resistance, and the influence of the different microstructural singularities on corrosion properties and mechanisms are systematically addressed further below.

Additionally, it is important to mention that passivity range in SLM as-built + SSP (570 mV_{Ag/AgCl}) also increased respect to the wrought + annealing series but nevertheless, it decreased in comparison to SLM as-built. Thus, polarization results also indicate that pitting resistance of SLM as-built series submitted to SSP is lower than SLM as-built, which might be attributed to the poor properties of the passive film, as will be discussed later. Anyway, it is also important to highlight that the influence of shot peening on corrosion resistance of AISI316L is often controversial in the literature [36,37] and the impact of the severe shot peening on corrosion resistance and mechanisms of SLM 316 L samples remains still unexplored. Several authors have observed that i_{pass} decreases and pitting potential (E_{pit}) increases with increasing compressive residual stresses in 316 L ASS, with residual stresses being introduced by laser shock processing [38] or cavitating jet [39]. However, detaching the effect of residual stresses from microstructure is in practice very challenging and it should be cautioned that techniques to alter residual stresses systematically affect microstructure. According to previous studies [39], the slightly lower interatomic distances, in the underlying compressively stressed metal lattice, led to i_{pass} to decrease, like in our work. Interestingly, in our study, severe shot peening was found to influence E_{pit} detrimentally (compared to the SLM as-built sample). As explained later, after the SSP treatment, the local surface stress gradient at the MPBs, with higher interfacial free energy, induces its decohesion, which affects the nature of the oxide passive film. Thus, the higher local free volume of MPBs seems to provide a fast mass transport pathway for the corrosive electrolyte, and corrosion attack occur severely along the MPBs. Aligned with [40], this fact contributes to justify the lower E_{pit} value found in the as-built + SSP sample, in comparison to that found in the SLM as-built series.



$$C = (Q \cdot R^{1-n})^{\frac{1}{n}} \quad (4)$$

$$t = \frac{\epsilon \cdot \epsilon_0 \cdot A}{C_f} \quad (5)$$

Fig. 13. Equivalent circuit diagram.

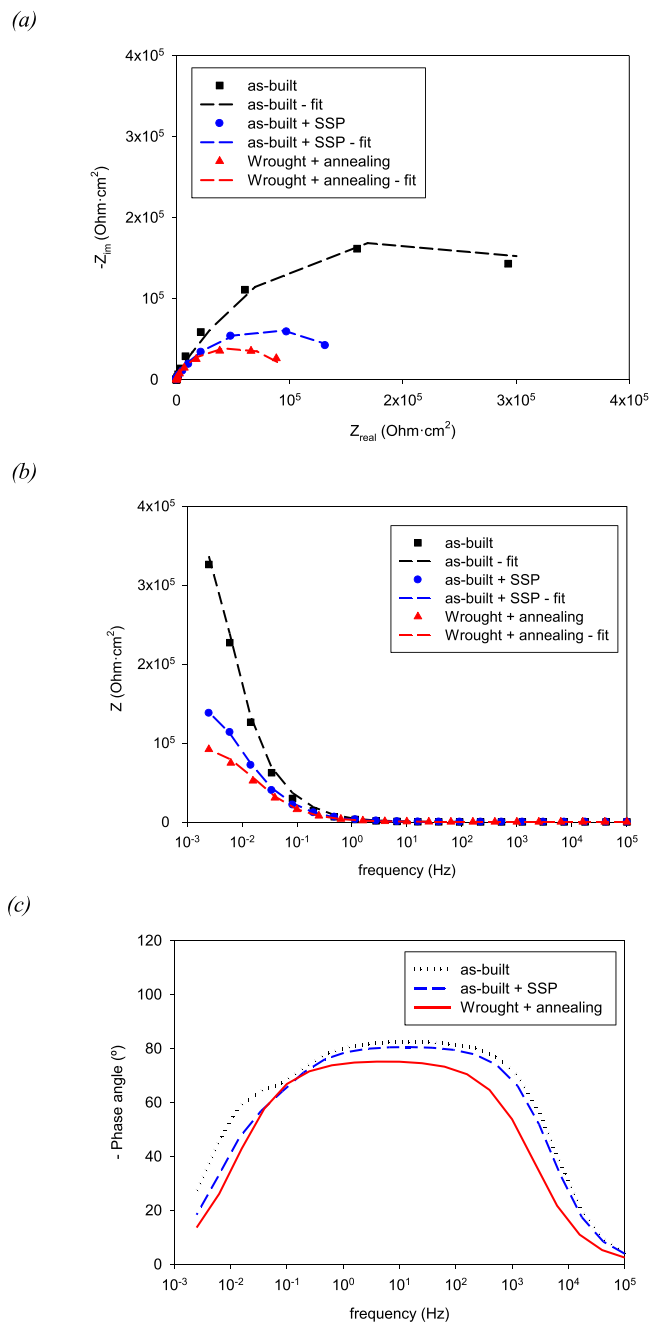


Fig. 14. (a) Nyquist plots. Bode plots: (b) Impedance-frequency curves and (c) the phase angle-frequency curves.

3.3.2. Potentiostatic polarization

Current versus time curves obtained from the potentiostatic polarization measurements are given in Fig. 12. The current of the different

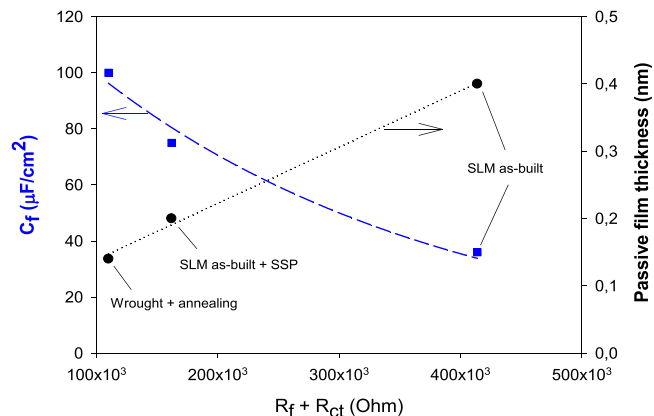


Fig. 15. C_f and passive film thickness evolution as a function of the overall polarization resistance.

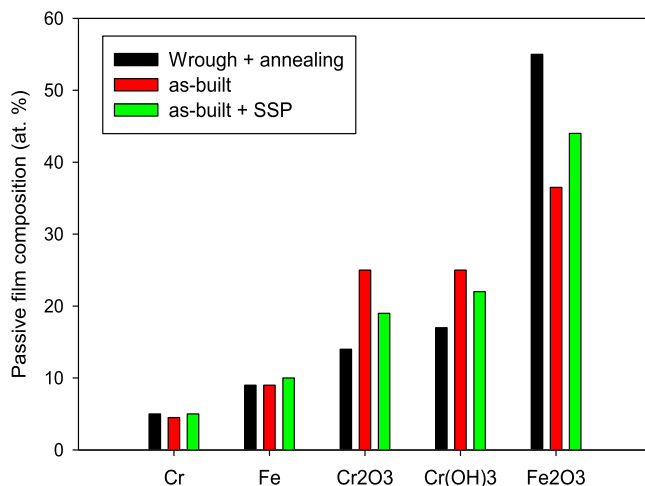


Fig. 16. Comparison of the composition of passive film formed on the wrought and SLM series (with and without SP) in 3.5 wt% NaCl.

series rapidly dropped because of the rapid passivation of the surface. The anodic current evolution of the SLM as-built and SLM as-built + SSP were stable, whereas that of the wrought + annealing series evidenced current instabilities associated to metastable pitting events. In that case, the shape of the current-time curve is associated to initiation, growth and repassivation of metastable pits. However, film stability notably increases in the selective laser melted series, even in the SLM as-built series submitted to severe shot peening. Thus, the anodic current density evolution and the metastable pitting events are in agreement with the potentiodynamic polarization results.

3.3.3. EIS measurements

The EIS measurements of SLM and wrought + annealing series are shown in Fig. 14 and the electrochemical parameter obtained from the

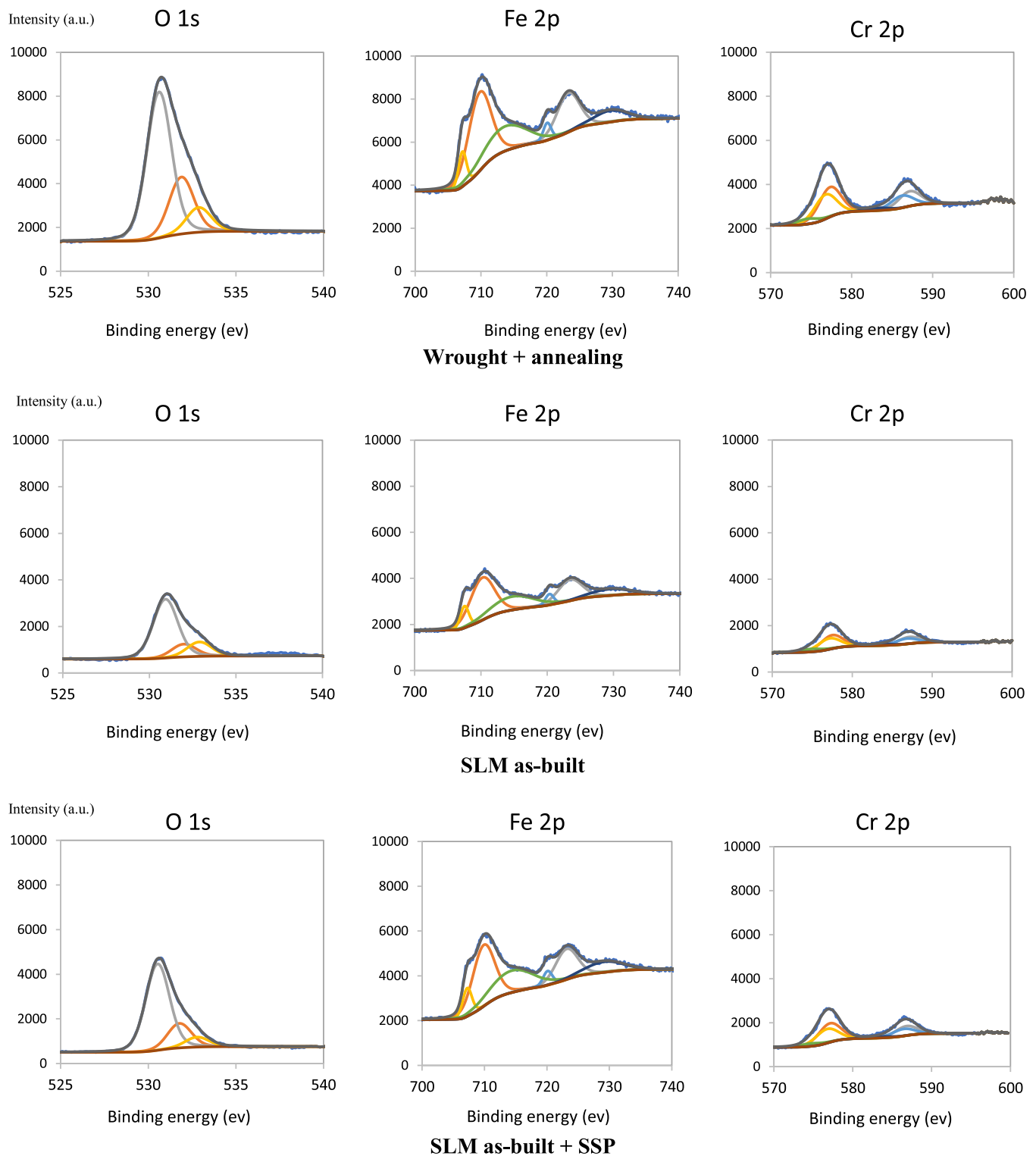


Fig. 17. XPS spectra of Fe and Cr for the passive film formed on the studied steel series.

EIS measurements are summarized in Table 8. SLM and wrought + annealing series show two capacitive loops, and the EIS plots were fitted by the equivalent circuit proposed in Fig. 13. J. Nie et al. [33] and Yang Zhao et al. [4] proposed a similar circuit to fit the EIS data, $R(Q[R(QR)])$, in an additively manufactured 316 L stainless steel in 3.5 wt% NaCl solution. In this equivalent circuit mode, R_s is the electrolyte resistance, Q_{dl} (C_{dl} , n_{dl}) is the double layer capacitance at the film/electrolyte interface, R_{ct} is the charge transfer resistance, Q_f (C_f , n_f) is

the passive film capacitance and R_f represents the resistance of the passive film. The capacitance (C) can be calculated according to equation 4. Based on this analysis, the thickness of the passive film (t) can be estimated using equation 5, where 'A' is the electrode surface area, ' ϵ ' is the dielectric constant of the oxide film (assumed to be Equal to 15.6 for Cr_2O_3 [41]) and ' ϵ_0 ' is the permittivity of the vacuum ($8.854 \cdot 10^{-14}$ F/cm [10]).

As can be seen in Fig. 14(a), SLM as-built series exhibited a large

Table 9

Binding energies of Cr 2p, Fe 2p and O 1 s by XPS analysis of the passive film on the wrought + annealing, as-built and as-built + SSP series after potentiostatic polarization in 3.5 % NaCl solution for 20 min.

Element	This study				Ref.
	wrought + annealing	as-built	as-built + SSP	Peak	
Cr	(2p _{3/2}) 574	(2p _{3/2}) 574	(2p _{3/2}) 574.5	Cr	[42]
	(2p _{1/2}) 583	(2p _{1/2}) 584	(2p _{1/2}) 583.3	Cr	[33]
	(2p _{3/2}) 576	(2p _{3/2}) 577	(2p _{3/2}) 577	Cr ₂ O ₃	[43]
	(2p _{3/2}) 577	(2p _{3/2}) 578	(2p _{3/2}) 577.3	Cr	[44]
	(2p _{1/2}) 586.3	(2p _{1/2}) 587	(2p _{1/2}) 586.8	(OH) ₃	[33]
	(2p _{1/2}) 587.4	(2p _{1/2}) 587.5	(2p _{1/2}) 587	Cr	[33]
	(2p _{1/2}) 587.5	(2p _{1/2}) 587	(2p _{1/2}) 587	(OH) ₃	[33]
Fe	(2p _{3/2}) 707	(2p _{3/2}) 707	(2p _{3/2}) 707.3	Fe	[45]
	(2p _{1/2}) 720.1	(2p _{1/2}) 720.2	(2p _{1/2}) 720.3	Fe	[33]
	(2p _{3/2}) 710	(2p _{3/2}) 710	(2p _{3/2}) 710	Fe ₂ O ₃	[45]
	(2p _{1/2}) 723	(2p _{1/2}) 723.5	(2p _{1/2}) 723.4	Fe ₂ O ₃	[33, 46]
	(2p _{1/2}) 723	(2p _{1/2}) 723.5	(2p _{1/2}) 723.4	Fe ₂ O ₃	[46]
O	531	531	530.7	O ₂	[33]
	532	532	531.8	OH	[33]
	533	533	532.9	H ₂ O	[47]

Table 10

Mechanical and microstructural features.

	HV ₂₀₀	GS (μm)	GND·10 ¹⁴ (m/m ³)	σ _{res} (MPa)	FWHM (°)	Hardened layer (μm)
Wrought & annealing	200	30	0.5	-100	1.0	-
SLM as-built	260	15	1.5	+ 300	1.4	-
SLM as-built + CSP	350	0.2	8	-450	2.6	50
SLM as-built + SSP	420	0.05	11	-700	3.5	100

HV: in the case of the samples submitted to shot peening, Vickers hardness was determined near the surface layer

GS: average grain size determined by EBSD. In the case of the shot peening, maximum grain refinement is indicated

GND: geometrically necessary dislocations.

σ_{res}: surface residual stress measured by XRD

FWHM: Full Width at Half Maximum determined by XRD

Hardened layer: it does reference to the layer depth affected by the mechanical shot peening treatment where grain refinement was promoted

capacitive loop radius what indicates higher corrosion resistance. According to this, polarization resistance (R_{ct}+R_f=414,000Ω) was the highest among the studied series. Additionally, barrier properties of the

Table 11

Results obtained from the electrochemical analysis and areas prone to corrosion attack.

	E _{corr} (V)	E _{pit} (V)	i _{pass} (μA/cm ²)	R _p (Ω)	Passive layer		Corrosion areas
					t (nm)	Cr ₂ O ₃ (XPS)	
Wrought & annealing	-0.21	0.13	0.04	110,000	0.14	15.0	MnS [13]
SLM as-built	-0.11	0.73	0.06	414,000	0.40	25.0	very locally at GBs
SLM as-built + SSP	-0.07	0.50	0.02	162,000	0.20	18.5	MPBs, GBs and subgrains

E_{corr}: corrosion potential

E_{pit}: pitting potential

i_{pass}: passive current density

R_p: overall polarization resistance (R_{ct}+R_f)

t: passive film thickness estimated according to equation 5

composition of the passive layer was determined from the XPS analysis

passive layer are associated with a high value of the impedance moduli at 10 mHz. As can be seen in Fig. 14(b), |Z|_{0.01 Hz} notably increased in the SLM as-built samples. As previously mentioned from the potentiodynamic polarization, the passivity range (E_{pit}-E_{corr} range) was particularly high in the SLM as-built series (Table 7). Based on the phase angle-frequency curves, see Fig. 14(c), the phase angles approaching to -90° from low to medium frequencies is associated to the formation and growth of a stable passive film [4]. SLM as-built series, with a phase angle value close to -90° over a certain frequency range, had higher corrosion resistance than that of wrought + annealing. The calculated passive film thickness of SLM as-built sample is 3 times thicker than that of the wrought + annealing. Fig. 15 shows the thickness and the capacitance of the passive layer, as a function of the overall polarization resistance (R_{ct} + R_f). Film capacitance, varying from 30 to 200 μF/cm², are representative of corroding iron surfaces [4,13,25]. Interfacial capacitance decreases as polarization resistance increases, resulting in a better stability of passive layer. As will be discussed later from the XPS analysis, SLM as-built series had a greater fraction stable oxides (Cr₂O₃). On the other hand, although corrosion resistance of the SLM as-built + SSP series was also greater than that of the wrought series, after applying the severe shot peening treatment, corrosion resistance decreased in comparison to the un-peened SLM as-built series. As will be discussed later, and in comparison to the un-peened SLM as-built series, high-energy delivered onto the steel surface seems to affect the nature of the passive film, which jeopardizes the passive film stability.

3.4. Composition of passive film. XPS results

The surface composition of passive film on wrought + annealing and SLM series (as-built and as-built + SSP) was analyzed by XPS. Composition of each element is shown in Fig. 16. The different species were calculated from the integral area of corresponding elements, which were deconvoluted from the high resolution XPS spectra (Fig. 17). In all the series, the presence of metal oxides, such as Fe₂O₃, Cr₂O₃ and Cr(OH)₃ was revealed. Table 9 shows the corresponding binding energies of the peaks.

The variations of each component can play an important role on corrosion resistance of the passive film. According to the results, in SLM as-built series, it is clear that stable metal oxide Cr₂O₃ is larger than others, while the unstable Fe₂O₃ decreased. Thus, it can be concluded that passive film of SLM as-built series had much more stability than that of the wrought + annealing and as-built + SSP series. It is important to recall that a thicker passive layer was formed in the as-built series, acting as a barrier to ion diffusion and protecting the substrate against further dissolution. In a previous work, Yang Zhao et al. [4] stated that metallurgical defects (i.e. grain boundaries) in selective laser melted 316 L enhances dissolution and releases a large quantity of Cr³⁺ ions at the interface, which causes precipitation and dehydration of Cr(OH)₃ to promote much more stable Cr₂O₃ oxides.

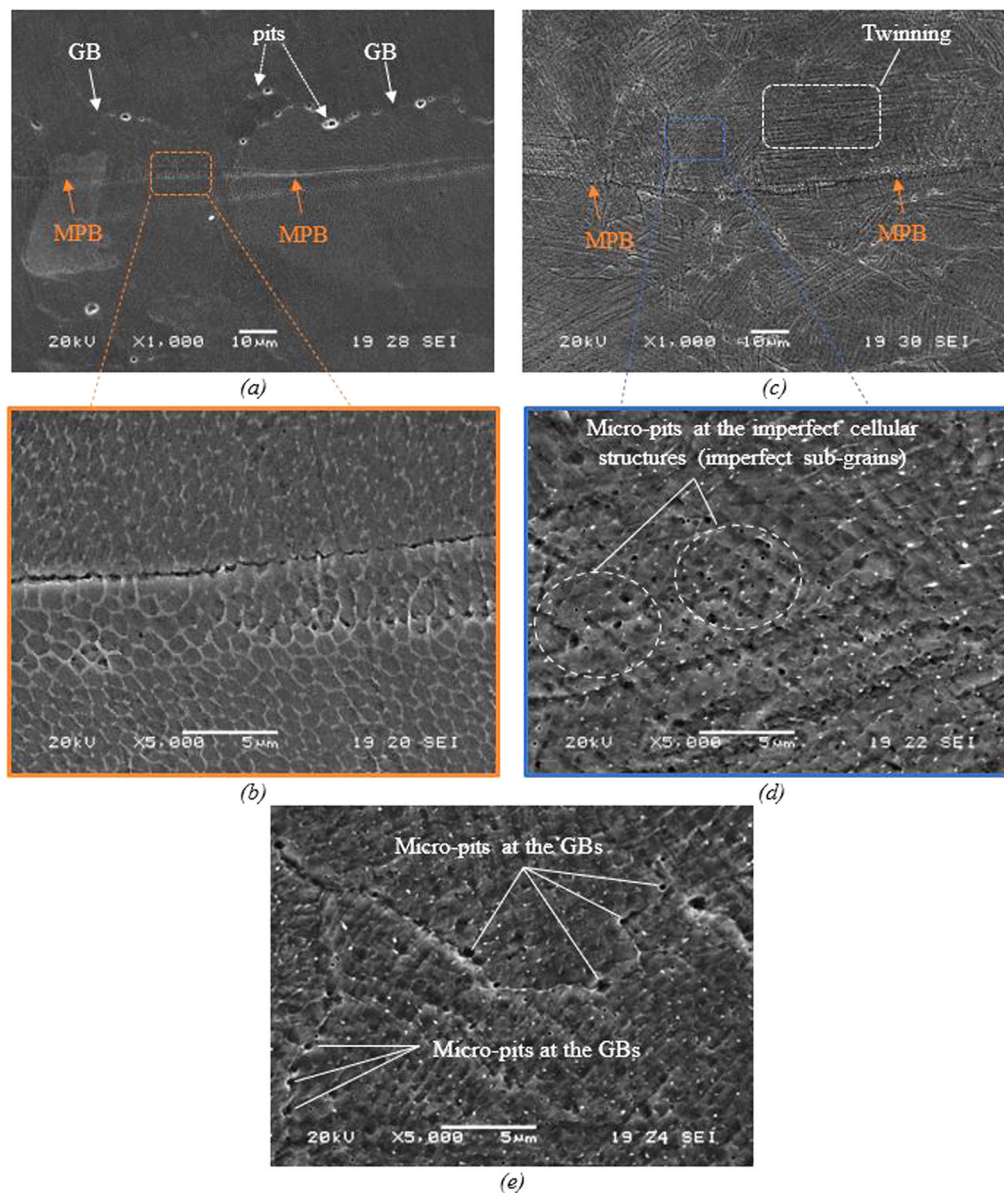


Fig. 18. Surface appearance after potentiostatic polarization test in +0.25 V vs. OCP. (a) and (b) SLM as-built. (c), (d) and (e) SLM as-built + SSP. 'GB' is the grain boundary and 'MPB' is the melt pool boundary.

4. Discussion

Several studies have demonstrated that 316 L made by selective laser melting has higher yield strength than conventional wrought 316 L steel. Nevertheless, regarding corrosion mechanisms and properties, controversial results have been found in the literature. On the one hand, Zhou et al. [48] and Sun et al. [49] demonstrated that general corrosion behavior of SLM 316 L is more prone to pitting corrosion attack. On the other hand, Xiao-qing Ni et al. [3] and Yang Zhao [4] reported that pitting potential of the SLM 316 L were higher than those of the wrought samples. Nie et al. [33] informed that additively manufactured 316 L exhibited better general corrosion resistance than wrought but pitting corrosion resistance was inferior to that of wrought 316 L. To solve these conflict points, microstructural and corrosion properties of the SLM 316 L stainless steel must be systematically studied. In particular, two question still remain: (1) how much do SLM microstructural features influence passive film stability, even after the application of the SSP treatment and (2) what are the potential nucleation pitting sites. To further discuss corrosion properties and mechanisms, mechanical and

microstructural changes promoted among the different series are summarized in Table 10, whilst corrosion results are shown in Table 11 likewise.

316 L ASS fabricated by conventional ingot metallurgy is was more sensitive to pitting corrosion than additively manufactured, when exposed to chloride containing environments. Wrought + annealing series had the worst corrosion resistance. However, SLM as-built exhibited a higher pitting potential than the wrought + annealing samples. This improvement in pitting resistance is attributed to the reduced size and content of detrimental manganese-sulphide (MnS) inclusions, during rapid solidification in the SLM process. It is well known that MnS inclusions act as potential pit initiation sites in austenitic stainless steels conventionally manufactured [50]. Sander et al. [6] stated that annihilation of MnS, in selective laser melted 316 L, promoted to homogeneous Cr composition of the oxide layer inclusions in the surrounding area, which increased the pitting potential and reduce the frequency of metastable pitting in 3.5 wt% NaCl.

In our study, the passive film thickness of SLM as-built was 3 times higher than wrought + annealing series. In a previous study, Kong et al.

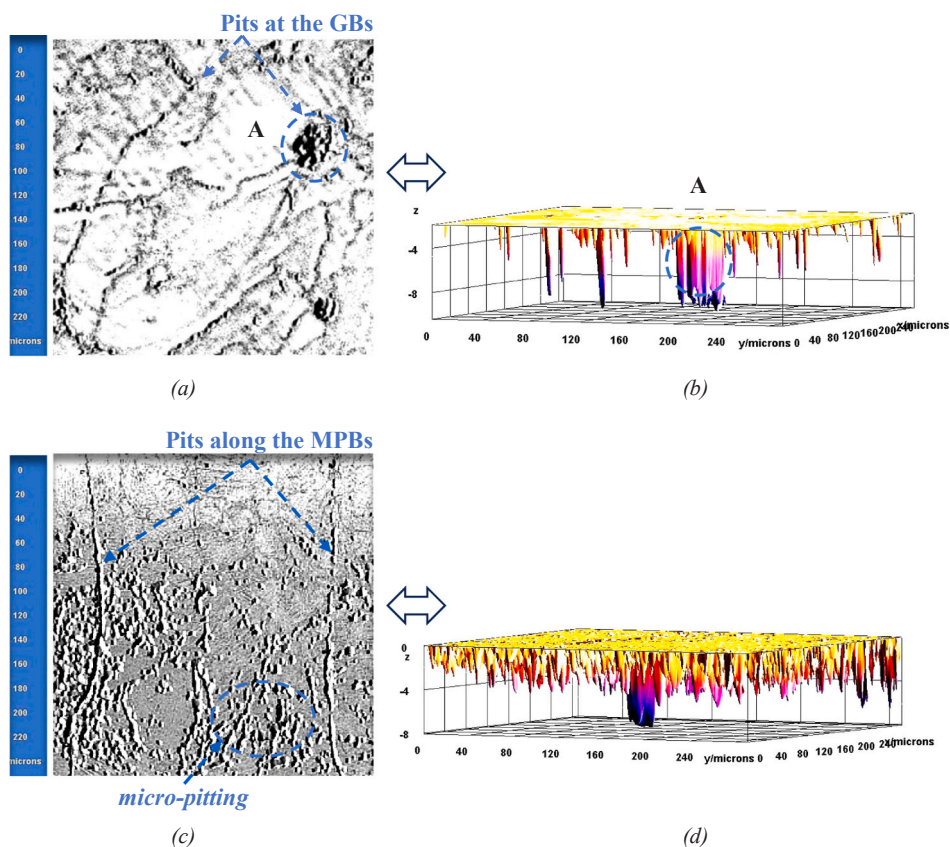


Fig. 19. Confocal analysis for deepest pits after potentiostatic polarization test in 3.5 wt% NaCl at +0.25 V vs. OCP. (a,b) SLM as-built. (c,d) SLM as-built + SSP.

[10] analyzed corrosion resistance of selective laser melted 316 L in 3.5 wt% NaCl solution. The thickness of the passive layer was found to be 0.44 nm, nearly to that determined in our work. In SLM as-built samples, a thicker passive layer is formed due to high dislocation density during the rapid solidification. GND density in the SLM as-built was estimated to be $1.5 \cdot 10^{14} \text{ m}^{-3}$, whereas it decreased to $0.5 \cdot 10^{14} \text{ m}^{-3}$ in the wrought + annealing series (Table 10). Additionally, grain morphology and grain sizes were compared using EBSD. SLM process promoted grain refinement, indicating that the SLM as-built grains tended to be in the range of $\sim 10\text{--}15 \mu\text{m}$ instead of $\sim 30 \mu\text{m}$ determined in the wrought + annealing samples (Fig. 3(a)). Definitely, in SLM as-built series, high fraction of grain boundaries promoted due to the grain refinement and cellular boundaries with an average size of $\sim 400 \text{ nm}$ (Fig. 2) are the areas having high dislocation density. Dislocations have high activation energy because of the localized lattice distortion, which is also confirmed by the increase of the FWHM parameter when SLM as-built and wrought series are compared. It seems dislocations favour elements to migrate by increasing the density of diffusion path and the chemically active dislocation in grain boundaries and cell boundaries promotes electron activity and diffusion. Thus, a thicker passive layer ($t = 0.4 \text{ nm}$ in Table 11) is formed due to the increased reactivity causes nucleation sites for oxidation. From the EIS analysis, the improved passive film resistance ($R_f = 320000 \Omega$) and charge transfer resistance ($R_{ct} = 94000 \Omega$) measured in the SLM as-built series contribute to reveal the best passive film stability, among the studied series. As previously stated, the angle phase close to -90 degrees (Fig. 14(c)) is associated with the formation and growth of a passive film. In this regard and unlike what had been observed in the wrought series (Fig. 12), anodic current instabilities, associated to metastable pitting events, were not observed either in the SLM as-built samples.

On the other hand, sample submitted to severe shot peening also

evidenced higher corrosion resistance than wrought + annealing series. In this case, the density of GND notably increased to $11 \cdot 10^{14} \text{ m}^{-3}$, near the shot peened surface. Additionally, SSP modified the grain size. EBSD analysis revealed the presence of nanograins (grain size $< 100 \text{ nm}$, Fig. 6) near the surface layer submitted to shot peening (12 A and 3000 % coverage). Nevertheless, it is important to recall that austenitic phase was totally stable despite of the high-energy delivered onto the steel surface, and the presence of strain-induced martensite was not revealed by XRD analysis (Fig. 5 and Fig. 9). Gundgire et al. [31] found a similar result, after applying shot peening in a 316 L steel additively manufactured. The additively manufactured samples did not have martensitic peaks even for the severely peened samples. This fact is associated to strongly orientated grain structure in the SLM samples, which are more resistant to plastic deformation.

Based on the previous explanation, the greatly smaller grain size and higher dislocations determined in the SLM as-built + SSP series should be expected to improve corrosion resistance. However, a thicker a more compact passive film was formed on the SLM as-built samples (without severe shot peening). Although several authors have observed that i_{pass} decreases with increasing compressive residual stresses, the compressive residual stresses could also decrease the defect concentration in the passive film and consequently, slow down its kinetics growth. In the SLM as-built + SSP samples, i_{pass} ($\sim 20 \text{ nA/cm}^2$) was slightly lower than that determined in the SLM as-built ($\sim 60 \text{ nA/cm}^2$), as explained above. However, high-energy transmitted to the surface seems to compromise the passive film stability. In this study, high level of compressive residual stresses (-700 MPa) were found to influence pitting potential detrimentally. A similar effect was also reported by Lei Guan et al. in a 316 L submitted to laser shock peening [40]. They found poor stability of the passivation film and a higher likelihood of a metastable pit transforming into a stable one in series subjected to laser shock peening. Here, we speculate that compressive residual stresses are more

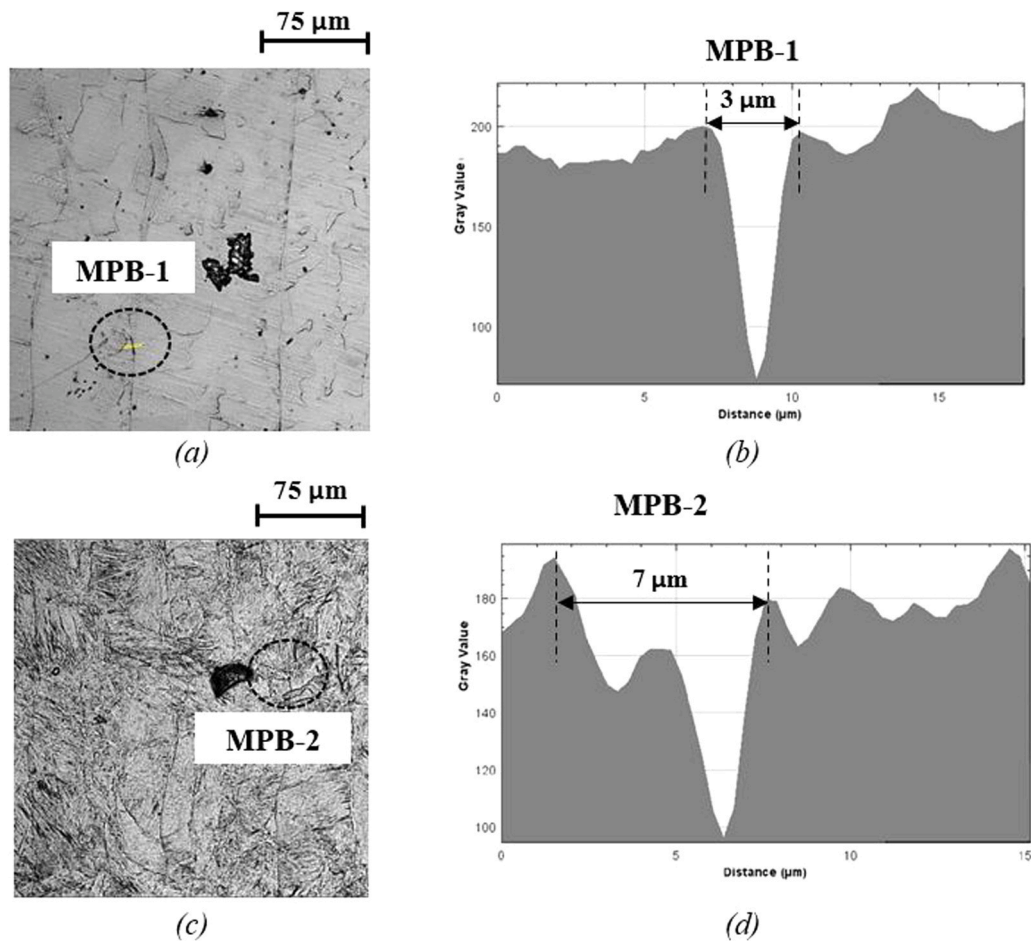


Fig. 20. Confocal analysis. (a) surface of the SLM as-built and (b) transversal profile along the MPB-1 of the SLM as-built series. (c) Surface of the SLM as-built + SSP and (d) transversal profile along the MPB-2 in the SLM as-built + SSP series.

dramatically devoted to the localized active sites rather than the microstructure of the passive film. The existence of microdefects and the uneven stress distribution along the MPBs (along with the induced local decohesions, Fig. 20) nullify the advantageous effects of compressive residual stress on the stability of the passive film during the growing process of metastable pits. Therefore, in SLM samples, the pitting potential decreased after the SSP treatment (Table 11).

Fig. 18 and Fig. 19 show the surface morphologies of SLM as-built series and SLM as-built + SSP after the potentiostatic polarization tests. In the case of the SLM as-built samples, local pits were observed at the grain boundaries (GB), whereas cells interiors and cellular boundaries remained practically intact, as can be seen in Fig. 18(a) and (b). However, after applying the SSP, micro-pitting nucleated to be the one of the main corrosion mechanisms and consequently, cells interiors were highly attacked, Fig. 18(d). It is important to highlight that cellular substructure became nearly invisible after the SSP, and twinning are now clearly visible (Fig. 18(c)). In a previous work, J. Sun et al. [12] also reported that deformation twins and dislocation break the cellular walls promoting the imperfect cell structure in a selective laser melted 316 L stainless steel submitted to ultrasonic severe surface rolling (USSR). In this study, the cell size was reported to be 449 nm. Nevertheless, after the applied severe plastic deformation, USSR showed a nanostructure with a grain size of 86 nm, resulting in a refined microstructure near the surface layer. In the present study, with 12 A intensity and 3000 % coverage (SSP), grain structure is refined to 50 nm in the upper layer (Fig. 6(d)). Thus, the induced grain refinement level was notably higher than cellular structure size (~400 nm, Fig. 2(f)). This factor along with the high-stress level led to a decrease in the passive film Cr_2O_3 content

and then, passive film stability was jeopardized.

To better observe the appearance of the corroded surface, sample's topography was also analyzed by means of the confocal microscope. We also observe that corrosion attack occurs severely along the MPBs in the SLM as-built + SSP samples (Fig. 19c). As can be seen in Fig. 20, due to the severe bombardment, the high-energy transmitted onto the steel surface seems to promote decohesion along the MPBs, in comparison to the un-peened one (SLM as-built). This phenomenon contribute to trigger pitting corrosion along the MPBs. These factors play a crucial role in accelerating the passive film destruction, when SLM as-built series was also submitted to SSP. The atomic arrangement is disordered at the MPB, which was an important crystal defect, likely due to the local variation in elemental distribution, porosity and residual stresses [48, 51]. The high-energy transmitted by the SSP could generate a local surface stress gradient at the MPB, which caused the MPBs to have higher interfacial free energy. The stress distribution at the MPBs was uneven and interfaces decohesion happen. The higher free interfacial energy seems to be beneficial to ion chemisorption and then, to decrease passive film stability in series submitted to SSP.

5. Conclusions

In this work, the microstructure and corrosion behavior of selective laser melted 316 L samples were systematically studied. Results are compared to those obtained in the wrought + annealing 316 L. The severe shot peened response of the additively manufactured 316 L austenitic stainless steel was also analyzed.

- Different from the typical microstructure of equiaxed grain of wrought + annealing 316 L, SLM 316 L (as-built) consists of finer grains and sub-grain boundaries. CSP and SSP produce a gradient surface layer. In the case of the SSP (12 A and 3000 % coverage), the gradient is thicker and the top surface layer has a nanostructure with an average grain size of 50 nm. The absence of strain-induced martensite was confirmed, even after the SSP treatment.
- The corrosion property of 316 L ASS in 3.5 wt% NaCl could be improved by the SLM process. Both the SLM (as-built and as-built + SSP) and wrought + annealing series composed of Fe₂O₃, Cr₂O₃, as well as some amorphous hydroxide Cr(OH)₃. A large number of sub-grain boundaries and the high dislocation density induce the formation of a thicker and more compact passive layer on SLM 316 L (as-built). SLM as-built series had a greater fraction of stable oxide Cr₂O₃ than wrought + annealing series.
- In comparison to the SLM as-built series, the passive film thickness and pitting potential decreased after the SSP treatment. Due to the severe bombardment with 12 A and 3000 % coverage, microgalvanic corrosion is mainly encouraged along the MPBs, resulting in a less pitting corrosion resistance. Anywise, general corrosion resistance of SLM as-built + SSP was also higher than that found in the wrought 316 L ASS.

To conclude, the results indicate that SSP promoted deeper grain refinement, increased hardness and led to higher and deeper residual stresses. Although the corrosion response of the SLM as-built submitted to severe plastic deformation was greater than that observed in the wrought 316 L steel, authors have planned to analyze and report corrosion response of SLM 316 L subjected to conventional shot peening treatments in further publications.

Author statement

All authors certify that they have participated sufficiently in the work to take public responsibility for the content, including participation in the concept, design, data analysis, writing, or revision of the manuscript.

- Conception and design of study: L.B. Peral and I. Fernández-Pariente.
- Acquisition of data: P. Ebrahimzadeh, L.B. Peral, R. González-Martínez.
- Analysis and/or interpretation of data: P. Ebrahimzadeh, L.B. Peral and E. Mardaras
- Drafting the manuscript: L.B. Peral, P. Ebrahimzadeh, R. González-Martínez.
- Revising the manuscript critically for important intellectual content: I. Fernández-Pariente, E. Mardaras, I.I. Cuesta and L.B. Peral

CRedit authorship contribution statement

I. Fernández-Pariente: Writing – review & editing, Writing – original draft, Supervision, Resources, Project administration, Methodology, Investigation, Funding acquisition, Conceptualization. **L.B. Peral:** Writing – review & editing, Writing – original draft, Validation, Supervision, Methodology, Investigation, Formal analysis, Data curation, Conceptualization. **R. González-Martínez:** Visualization, Validation, Investigation, Formal analysis, Data curation. **E. Mardaras:** Writing – original draft, Validation, Resources, Investigation. **I.I. Cuesta:** Resources, Project administration, Investigation, Funding acquisition. **P. Ebrahimzadeh:** Writing – original draft, Visualization, Methodology, Investigation, Formal analysis, Data curation.

Declaration of Competing Interest

The authors declare that they have no known competing financial

interests or personal relationships that could have appeared to influence the work reported in this paper.

Acknowledgments

The authors would like to thank the Spanish Government for the financial support received to perform Project TED2021-130306B-100 (Safe-Wind). The authors are also grateful for the funding received from the MICINN PID2021-124768OB-C21 and TED2021-130413B-100 projects, co-financed with Next Generation EU funds.

Data Availability

Data will be made available on request.

References

- [1] E. Ura-Bińczyk, A. Dobkowska, P. Bazarnik, J. Ciftci, A. Krawczyńska, W. Chromiński, et al., Effect of annealing on the mechanical and corrosion properties of 316L stainless steel manufactured by laser powder bed fusion, *Mater. Sci. Eng.: A* 860 (2022) 144263, <https://doi.org/10.1016/j.msea.2022.144263>.
- [2] M. Al-Amin, A.M. Abdul-Rani, M. Rana, S. Hastuty, M. Danish, S. Rubaiee, et al., Evaluation of modified 316L surface properties through HAP suspended EDM process for biomedical application, *Surf. Interfaces* 28 (2022) 101600, <https://doi.org/10.1016/j.surf.2021.101600>.
- [3] X. Ni, D. Kong, Y. Wen, L. Zhang, W. Wu, B. He, et al., Anisotropy in mechanical properties and corrosion resistance of 316L stainless steel fabricated by selective laser melting, *Int. J. Miner., Metall., Mater.* 26 (2019) 319–328, <https://doi.org/10.1007/s12613-019-1740-x>.
- [4] Y. Zhao, H. Xiong, X. Li, W. Qi, J. Wang, Y. Hua, et al., Improved corrosion performance of selective laser melted stainless steel 316L in the deep-sea environment, *Corros. Commun.* 2 (2021) 55–62, <https://doi.org/10.1016/j.corcom.2021.09.002>.
- [5] Z. Sun, X. Tan, S.B. Tor, W.Y. Yeong, Selective laser melting of stainless steel 316L with low porosity and high build rates, *Mater. Des.* 104 (2016) 197–204, <https://doi.org/10.1016/j.matdes.2016.05.035>.
- [6] G. Sander, S. Thomas, V. Cruz, M. Jurg, N. Birbilis, X. Gao, et al., On The Corrosion and Metastable Pitting Characteristics of 316L Stainless Steel Produced by Selective Laser Melting, *J. Electrochem Soc.* 164 (2017) C250–C257, <https://doi.org/10.1149/2.0551706jes>.
- [7] Q. Chao, V. Cruz, S. Thomas, N. Birbilis, P. Collins, A. Taylor, et al., On the enhanced corrosion resistance of a selective laser melted austenitic stainless steel, *Scr. Mater.* 141 (2017) 94–98, <https://doi.org/10.1016/j.scriptamat.2017.07.037>.
- [8] B. Zhang, J. Wang, B. Wu, Y.T. Zhou, X.L. Ma, Quasi-in-situ ex-polarized TEM observation on dissolution of MnS inclusions and metastable pitting of austenitic stainless steel, *Corros. Sci.* 100 (2015) 295–305, <https://doi.org/10.1016/j.corsci.2015.08.009>.
- [9] M. Ziętala, T. Durejko, M. Polański, I. Kunce, T. Pociński, W. Zieliński, et al., The microstructure, mechanical properties and corrosion resistance of 316L stainless steel fabricated using laser engineered net shaping, *Mater. Sci. Eng.: A* 677 (2016) 1–10, <https://doi.org/10.1016/j.msea.2016.09.028>.
- [10] D. Kong, C. Dong, X. Ni, L. Zhang, J. Yao, C. Man, et al., Mechanical properties and corrosion behavior of selective laser melted 316L stainless steel after different heat treatment processes, *J. Mater. Sci. Technol.* 35 (2019) 1499–1507, <https://doi.org/10.1016/j.jmst.2019.03.003>.
- [11] V. Cruz, Q. Chao, N. Birbilis, D. Fabijanic, P.D. Hodgson, S. Thomas, Electrochemical studies on the effect of residual stress on the corrosion of 316L manufactured by selective laser melting, *Corros. Sci.* 164 (2020) 108314, <https://doi.org/10.1016/j.corsci.2019.108314>.
- [12] J. Sun, Q. Sun, Y. Liu, B. Li, Z. Zhang, B. Xu, et al., Improving corrosion resistance of selective laser melted 316L stainless steel through ultrasonic severe surface rolling, *J. Mater. Res. Technol.* 20 (2022) 4378–4391, <https://doi.org/10.1016/j.jmrt.2022.09.011>.
- [13] P. Ebrahimzadeh, L.B. Peral, R. González-Martínez, E. Mardaras, I. Fernández-Pariente, Influence of severe surface plastic deformation induced by shot peening on microstructure and corrosion resistance of fine grained 316 L stainless steel, *Corros. Sci.* 231 (2024) 111988, <https://doi.org/10.1016/j.corsci.2024.111988>.
- [14] S. Bagherifard, S. Slawik, I. Fernández-Pariente, C. Pauly, F. Mücklich, M. Guagliano, Nanoscale surface modification of AISI 316L stainless steel by severe shot peening, *Mater. Des.* 102 (2016) 68–77, <https://doi.org/10.1016/j.matdes.2016.03.162>.
- [15] H. Zhang, S. Cao, B. Li, X. Li, C. Li, Shot peening coverage effect on laser powder bed fused steel, *Int. J. Mech. Sci.* 277 (2024) 109520, <https://doi.org/10.1016/j.ijmecsci.2024.109520>.
- [16] P. Ebrahimzadeh, L.B.P. Martínez, I.F. Pariente, F.J.B. Varela, Optimization of shot-peening parameters for steel AISI 316L via response surface methodology (RSM): introducing two novel mechanical aspects, *Int. J. Adv. Manuf. Technol.* 132 (2024) 647–667, <https://doi.org/10.1007/s00170-024-13274-8>.
- [17] K. Hajizadeh, H. Maleki-Ghaleh, A. Arabi, Y. Behnamian, E. Aghaie, A. Farrokhi, et al., Corrosion and biological behavior of nanostructured 316L stainless steel

- processed by severe plastic deformation, *Surf. Interface Anal.* 47 (2015) 978–985, <https://doi.org/10.1002/sia.5806>.
- [18] F. Yazdani, S.M. Rabiee, R. Jamaati, Comparison of conventional and severe shot peening effects on the microstructure, texture, roughness, hardness, and electrochemical behavior of austenitic stainless steel, *Heliyon* 10 (2024) e31284, <https://doi.org/10.1016/j.heliyon.2024.e31284>.
- [19] S. Pour-Ali, S. Mahdavi, S. Moradi, R. Tavangar, Effect of high-energy shot peening on the corrosion behavior and chloride threshold concentration of AISI 316L stainless steel rebar in simulated concrete pore solution, *J. Mater. Res. Technol.* 30 (2024) 2051–2063, <https://doi.org/10.1016/j.jmrt.2024.03.230>.
- [20] Q. Xu, D. Jiang, J. Zhou, Z. Qiu, X. Yang, Enhanced corrosion resistance of laser additive manufactured 316L stainless steel by ultrasonic surface rolling process, *Surf. Coat. Technol.* 454 (2023) 129187, <https://doi.org/10.1016/j.surfcoat.2022.129187>.
- [21] S. Geng, J. Sun, L. Guo, Effect of sandblasting and subsequent acid pickling and passivation on the microstructure and corrosion behavior of 316L stainless steel, *Mater. Des.* 88 (2015) 1–7, <https://doi.org/10.1016/j.matdes.2015.08.113>.
- [22] Y. Hao, B. Deng, C. Zhong, Y. Jiang, J. Li, Effect of surface mechanical attrition treatment on corrosion behavior of 316 stainless steel, *J. Iron Steel Res. Int.* 16 (2009) 68–72, [https://doi.org/10.1016/S1006-706X\(09\)60030-3](https://doi.org/10.1016/S1006-706X(09)60030-3).
- [23] L.B. Peral, A. Zafra, S. Bagherifard, M. Guagliano, I. Fernández-Pariente, Effect of warm shot peening treatments on surface properties and corrosion behavior of AZ31 magnesium alloy, *Surf. Coat. Technol.* 401 (2020) 126285, <https://doi.org/10.1016/j.surfcoat.2020.126285>.
- [24] M. Godec, S. Zaefferer, B. Podgornik, M. Šinko, E. Tchernychova, Quantitative multiscale correlative microstructure analysis of additive manufacturing of stainless steel 316L processed by selective laser melting, *Mater. Charact.* 160 (2020) 110074, <https://doi.org/10.1016/j.matchar.2019.110074>.
- [25] L.B. Peral, P. Ebrahimzadeh, A. Gutiérrez, I. Fernández-Pariente, Effect of tempering temperature and grain refinement induced by severe shot peening on the corrosion behavior of a low alloy steel, *J. Electroanal. Chem.* 932 (2023) 117207, <https://doi.org/10.1016/j.jelechem.2023.117207>.
- [26] B. Zhang, Y. Li, Q. Bai, Defect formation mechanisms in selective laser melting: a review, *Chin. J. Mech. Eng.* 30 (2017) 515–527, <https://doi.org/10.1007/s10033-017-0121-5>.
- [27] G. Álvarez, Z. Harris, K. Wada, C. Rodríguez, E. Martínez-Pañeda, Hydrogen embrittlement susceptibility of additively manufactured 316L stainless steel: Influence of post-processing, printing direction, temperature and pre-straining, *Addit. Manuf.* 78 (2023), <https://doi.org/10.1016/j.addma.2023.103834>.
- [28] Y. Zhang, F. Liu, J. Chen, Y. Yuan, Effects of surface quality on corrosion resistance of 316L stainless steel parts manufactured via SLM, *J. Laser Appl.* 29 (2017), <https://doi.org/10.2351/1.4983263>.
- [29] Z. Sun, X. Tan, S.B. Tor, W.Y. Yeong, Selective laser melting of stainless steel 316L with low porosity and high build rates, *Mater. Des.* 104 (2016) 197–204, <https://doi.org/10.1016/j.matdes.2016.05.035>.
- [30] T. Das, A. Erdogan, B. Kursuncu, E. Maleki, O. Unal, Effect of severe vibratory peening on microstructural and tribological properties of hot rolled AISI 1020 mild steel, *Surf. Coat. Technol.* 403 (2020) 126383, <https://doi.org/10.1016/j.surfcoat.2020.126383>.
- [31] T. Gundgire, T. Jokiah, S. Santa-aho, T. Rautio, A. Järvenpää, M. Vippola, Comparative study of additively manufactured and reference 316 L stainless steel samples – effect of severe shot peening on microstructure and residual stresses, *Mater. Charact.* 191 (2022) 112162, <https://doi.org/10.1016/j.matchar.2022.112162>.
- [32] L. Wei, Y. Liu, Q. Li, Y.F. Cheng, Effect of roughness on general corrosion and pitting of (FeCoCrNi)_{0.89}(WC)_{0.11} high-entropy alloy composite in 3.5 wt% NaCl solution, *Corros. Sci.* 146 (2019) 44–57, <https://doi.org/10.1016/j.corsci.2018.10.025>.
- [33] J. Nie, L. Wei, Y. Jiang, Q. Li, H. Luo, Corrosion mechanism of additively manufactured 316 L stainless steel in 3.5 wt% NaCl solution, *Mater. Today Commun.* 26 (2021) 101648, <https://doi.org/10.1016/j.mtcomm.2020.101648>.
- [34] R.F. Schaller, J.M. Taylor, J. Rodelas, E.J. Schindelholz, Corrosion properties of powder bed fusion additively manufactured 17-4 PH Stainless Steel, *Corrosion* 73 (2017) 796–807, <https://doi.org/10.5006/2365>.
- [35] D. Kong, X. Ni, C. Dong, L. Zhang, C. Man, J. Yao, et al., Heat treatment effect on the microstructure and corrosion behavior of 316L stainless steel fabricated by selective laser melting for proton exchange membrane fuel cells, *Electro Acta* 276 (2018) 293–303, <https://doi.org/10.1016/j.electacta.2018.04.188>.
- [36] A.A. Ahmed, M. Mhaede, M. Basha, M. Wollmann, L. Wagner, The effect of shot peening parameters and hydroxyapatite coating on surface properties and corrosion behavior of medical grade AISI 316L stainless steel, *Surf. Coat. Technol.* 280 (2015) 347–358, <https://doi.org/10.1016/j.surfcoat.2015.09.026>.
- [37] X. Chen, Y. Li, Y. Zhu, Y. Bai, B. Yang, Improved corrosion resistance of 316LN stainless steel performed by rotationally accelerated shot peening, *Appl. Surf. Sci.* 481 (2019) 1305–1312, <https://doi.org/10.1016/j.apsusc.2019.03.256>.
- [38] P. Peyre, C. Carboni, P. Forget, G. Beranger, C. Lemaitre, D. Stuart, Influence of thermal and mechanical surface modifications induced by laser shock processing on the initiation of corrosion pits in 316L stainless steel, *J. Mater. Sci.* 42 (2007) 6866–6877, <https://doi.org/10.1007/s10853-007-1502-4>.
- [39] O. Takakuwa, H. Soyama, Effect of Residual Stress on the Corrosion Behavior of Austenitic Stainless Steel, *Adv. Chem. Eng. Sci.* 05 (2015) 62–71, <https://doi.org/10.4236/aces.2015.51007>.
- [40] L. Guan, Z.-X. Ye, X.-Y. Yang, J.-M. Cai, Y. Li, Y. Li, et al., Pitting resistance of 316 stainless steel after laser shock peening: Determinants of microstructural and mechanical modifications, *J. Mater. Process Technol.* 294 (2021) 117091, <https://doi.org/10.1016/j.jmatprotec.2021.117091>.
- [41] A. Fattah-hosseini, M.A. Golozar, A. Saatchi, K. Raeissi, Effect of solution concentration on semiconducting properties of passive films formed on austenitic stainless steels, *Corros. Sci.* 52 (2010) 205–209, <https://doi.org/10.1016/j.corsci.2009.09.003>.
- [42] W.S. Zhang, E. Brück, Z.D. Zhang, O. Tegus, W.F. Li, P.Z. Si, et al., Structure and magnetic properties of Cr nanoparticles and Cr₂O₃ nanoparticles, *Phys. B Condens Matter* 358 (2005) 332–338, <https://doi.org/10.1016/j.physb.2005.01.469>.
- [43] H. Liu, D. Xu, K. Yang, H. Liu, Y.F. Cheng, Corrosion of antibacterial Cu-bearing 316L stainless steels in the presence of sulfate reducing bacteria, *Corros. Sci.* 132 (2018) 46–55, <https://doi.org/10.1016/j.corsci.2017.12.006>.
- [44] S.K. Bonagani, V. Bathula, V. Kain, Influence of tempering treatment on microstructure and pitting corrosion of 13 wt% Cr martensitic stainless steel, *Corros. Sci.* 131 (2018) 340–354, <https://doi.org/10.1016/j.corsci.2017.12.012>.
- [45] C. Man, C. Dong, T. Liu, D. Kong, D. Wang, X. Li, The enhancement of microstructure on the passive and pitting behaviors of selective laser melting 316L SS in simulated body fluid, 193–205, *Appl. Surf. Sci.* (2019) 467–468, <https://doi.org/10.1016/j.apsusc.2018.10.150>.
- [46] Y. Hua, R. Barker, A. Neville, The effect of O₂ content on the corrosion behaviour of X65 and 5Cr in water-containing supercritical CO₂ environments, *Appl. Surf. Sci.* 356 (2015) 499–511, <https://doi.org/10.1016/j.apsusc.2015.08.116>.
- [47] Q. Luo, Z. Qin, Z. Wu, B. Shen, L. Liu, W. Hu, The corrosion behavior of Ni-Cu gradient layer on the nickel aluminum-bronze (NAB) alloy, *Corros. Sci.* 138 (2018) 8–19, <https://doi.org/10.1016/j.corsci.2018.03.050>.
- [48] C. Zhou, S. Hu, Q. Shi, H. Tao, Y. Song, J. Zheng, et al., Improvement of corrosion resistance of SS316L manufactured by selective laser melting through subcritical annealing, *Corros. Sci.* 164 (2020) 108353, <https://doi.org/10.1016/j.corsci.2019.108353>.
- [49] Y. Sun, A. Moroz, K. Alrbaey, Sliding wear characteristics and corrosion behaviour of selective laser melted 316L stainless steel, *J. Mater. Eng. Perform.* 23 (2014) 518–526, <https://doi.org/10.1007/s11665-013-0784-8>.
- [50] A. Pardo, M.C. Merino, A.E. Coy, F. Viejo, R. Arrabal, E. Matykina, Pitting corrosion behaviour of austenitic stainless steels – combining effects of Mn and Mo additions, *Corros. Sci.* 50 (2008) 1796–1806, <https://doi.org/10.1016/j.corsci.2008.04.005>.
- [51] C. Zhao, Y. Bai, Y. Zhang, X. Wang, J.M. Xue, H. Wang, Influence of scanning strategy and building direction on microstructure and corrosion behaviour of selective laser melted 316L stainless steel, *Mater. Des.* 209 (2021) 109999, <https://doi.org/10.1016/j.matdes.2021.109999>.